2006

Simulations of a modified micro-scale electrophoretron

Nada Elmajdoub
Louisiana State University and Agricultural and Mechanical College, nelmaj1@lsu.edu

SIMULATIONS OF A MODIFIED MICRO-SCALE ELECTROPHORETRON

A Thesis

Submitted to the Graduate Faculty of the
Louisiana State University and
Agricultural and Mechanical College
In partial fulfillment of the
requirements for the degree of
Master of Science in Mechanical Engineering

in

The Department of Mechanical Engineering

by
Nada Elmajdoub
Ms., ENSICA (Toulouse), France, 2006
December, 2006

Acknowledgments

My research could have never been completed without my graduate advisor, Dr.Dimitris Nikitopoulos, who offered motivation, funding and personal support throughout the project. His genuine interest in my work, his can-do attitude and his optimistic prospective made our collaboration a big success. I am honored and delighted that Dr. Michael Murphy and Dr. Steven Soper accepted my invitation to be part of my committee.

In the chemistry department I was pleased to work with Dr.Hamed Shadpour, Dr.Malgorzata Witek and Dr.Mateusz Hupert. I am grateful for their help, knowledge, and patience in using the chemistry lab. I would like to thank Sudheer Rani, Vamsi and Amit for their help and support through the dark moments of research and also for providing a very nice working atmosphere.

I would like to give a special thanks to Simo, Pierre, Najib, Yassine, Amine, Ardita, Hicham, Dinesh, Izabela, Denada, Virginie, Julie and Moeb.

Everything came together through the financial support from the National Science Foundation and the National Institute of Health, which supplied research grants to Dr.Nikitopoulos and Dr.Soper's team.

Finally, I am eternally grateful to Mama and Baba, Mouna and Youssef for their outstanding continuous support and Love.

Table of Contents

List of Tables

List of Figures

Abstract

This paper presents theoretical analysis and numerical simulations of a modified micro-scale electrophoretron adapted for cycling reaction applications (PCR, LDR…). The electrophoretron consists of a closed-loop microchannel. If one part of the length of the channel has an electroosmotic mobility of an opposite sign than the remaining part, a continuous cyclic motion of the fluid can be sustained if a potential difference is applied on two electrodes strategically placed along the channel. Conservation of mass leads to the formation of a pressure gradient and a related hydrodynamic flow. Under appropriate combination of design parameters, the combined Electroosmotic –hydrodynamic flow contributes to the generation of continuous circular motion of the bulk of the fluid along the closed-loop channel.

The benefits of this technology for application to thermal cycling reactors are considerable. For example it eliminates long channel lengths required for a specified number of reaction cycles in a continuous flow device; this eliminates the associated high pressure drop in pressure driven continuous flow cycling reactors, and the associated high-voltage requirement in electrokinetically driven flow cycling reactors. It can also minimize thermal transition and cycling times because it allows the use of steady normal zones and provides the option of controlling the number of cycles necessary to obtain results without changing the architecture of the chip.

Chapter 1 Introduction

This work is part of a large research program whose goal is to develop integrated micro-analytical instrumentation for clinical diagnostics, genotyping and DNA sequencing. The instrument under development will be useful for the realization of multiplexed Polymerase Chain Reactions (PCR) and/or Ligase Detection Reactions (LDR) with electrokinetically driven flow.

The polymerase chain reaction (PCR) is a powerful tool for creating large numbers of copies of specific DNA fragments for both sequencing and genotyping applications. PCR is capable of rapidly amplifying a single DNA molecule into billions of identical molecules. This could be quite useful when working with low abundant targets. The common devices used for PCR are metal blocks that are continuously thermal cycled between the different temperatures required for the amplification process to occur. The particular advantage about these thermal cycles is that they can simultaneously amplify up to 384 samples placed in titer wells that are sandwiched between the cover plate and the thermal block. The disadvantage of such devices is the bad heat transfer management that is a consequence of managing a huge amount of thermal masses and the slow thermal transfer between the liquid and the titer well and the heating block. This is not very convenient and results in low process speed in addition to the reduction imposed by the thermal block in terms of the volume of the PCR cocktail due to the need of manually pipetting reagents into the wells.

In the literature there are two major types of PCR devices realized on the microscale, the chamber type and the continuous flow type.

Several micro chamber PCR devices have been reported. Researchers used different substrate materials, micro-fabrication technology and heating/cooling methods to achieve faster amplification performance. Daniel et.al (1998) micro-machined a silicon substrate using anisotropic wet etching. The heater and sensor were made using thin film platinum resistors connected to a computer running LabView software. The merit of this design was to decrease the thermal capacitance and increase the cooling rate. The total number of cycles for this device was 30. Preheating or postheating was realized for one minute.

Giordano et.al (2001) made a micro chamber PCR reactor with infrared mediated temperature control on a polyimide substrate. A tungsten lamp was used as a heat source and was focused on the micro-chamber through a convex lens. 15 cycles were completed in 240 seconds.

Kopp et. Al (1998) reported the first CFPCR reactor, they used glass as a substrate with an independent copper block for each temperature zone. PCR results for 20 cycles were obtained after 18.7mn. Mitchell et.al (2003) fabricated a CFPCR using LIGA and UV-LIGA to make mold inserts that were hot-embossed in polycarbonate, commercial heaters were used for each temperature and the cooling was performed through natural convection, with PID control of the temperature in each zone. Finite element simulations were used to investigate the design parameters and the thermal performance.

In micro chamber PCR devices, the DNA cocktail remains in a single chamber when heating and cooling elements are repeatedly thermally cycled. One advantage of the micro chamber PCR is that the chemical reagent volume is solely controlled by the size of the chamber and the chemical reaction requirements. However the chamber containing the DNA cocktail must also be heated and cooled, potentially slowing down the overall

thermal cycling rate due to the thermal capacitance of the device. On the other hand, continuous flow PCR (CFPCR) takes advantage of the low thermal capacitance and high thermal conductivity of the DNA sample in the micro-channels, allowing it to quickly reach thermal equilibrium with the channel's walls in each temperature zone before entering the next one. This accelerates the PCR process. However, the amount of reagent needed for the CFPCR is much greater than what is typically required for the micro chamber PCR, because the entire CFPCR channel must be filled. Those two kinds of PCR reactors are different from a drive mechanism point of view. The CFPCR reactors are pressure driven . The benefits of pressure drive includes ease of operation and reliability, providing ways to connect the PCR reactor with other downstream processing. The disadvantages are the back pressure generated during the flow through the micro-channel. Bonding and connection in pressure-driven chips must survive to this back pressure. The laminar hyperbolic flow profile is also a problem that encourages the diffusion phenomena and leads to dispersion of the sample. PCR is generally followed by LDR and capillary electrophoretic separation, which is performed electrokinetically and it is not straightforward to connect a pressure driven system with an electrokinetically driven one.

That's how researchers came to think about the necessity to investigate making a continuous flow PCR system, electrokinetically driven, that would alleviate some limitations related to the pressure driven devices such as minimization of sample diffusion phenomena due to the plug flow geometry, elimination of the need of the external pumping systems, ease to couple the system with the electrokinetical downstream processing, and negligible pressure drops induced by the plug's motion.

If one uses a straight channel to shuttle a DNA template electrokinetically, with a reasonable speed, in a fairly short CFPCR channel, a relatively large voltage has to be applied. This could lead to transverse electrical fields of several hundred thousands volts per centimeter between adjacent tracks in a spiral or serpentine configuration causing the creation of field free regions (equipotent zones). So a straight channel is not the best choice for this type of applications

Chen et.al (2005) managed to set up a novel electrokinetically driven synchronized PCR chip. This chip allowed DNA amplification to be carried out in a continuous flow mode using synchronized electrokinetic pumping. This design alleviated a lot of problems related to the pressure driven flow devices. Namely, leakage due to high back-pressure, diffusion due to the hyperbolic flow profile, the need of off-chip pumping systems.

Choi et al. (2001) demonstrated the construction of a capillary separation device for chromatography applications that they called “electrophoretron” in which the samples travels around a closed loop under the action of electroosmotic flow. This device was made of two capillaries, each of which had different surface preparations on their inside walls, such that the EOF is reversed from one chamber to the other, that were joined together to form a closed loop, and electrodes were placed inside two reservoirs When the loop was filled with buffer and a potential difference was applied between the two electrodes a circulating flow of liquid was established inside the loop because the flow rate was unequal in going from one electrode to another in clockwise versus a counterclockwise direction. Consequently a sample injected into this device, repeatedly

circulates between the two electrodes and the capillary separation column becomes effectively one of unlimited length.

This work is about providing proof of concept and feasibility of a continuous flow PCR micro-fluidic device that would use the electrophoretron principle to achieve thermal cycling in a closed loop micro-channel. Part of the channel length surface is modified with a dynamic coating to reverse the EOF in order to achieve continuous flow with no re-circulating flow regions and little velocity profile distortion induced diffusion of the DNA template. The length of the modified portion of the channel is determined judiciously to make the pressure gradient tend to zero in the whole channel and ensure cyclic flow with a nearly flat velocity profile. This has been done so as to alleviate issues related to an induced hydrodynamic flow profile. An optimal design in terms of the proportions between the channel mobility magnitudes and lengths necessary to realize the above conditions. The simple analysis is based on an analytical solution of electroosmotic flow in channels of circular crossection. Therefore, numerical simulations are carried out to investigate optimum design for rectangular crossection channels, which are more relevant to the micro-chip application. In these simulations combined electroosmotic and electrophoretic flow of charged species is simulated to examine the device capability in securing a circulating motion of charged (DNA) species. The theoretical study also showed that the principle is still applicable even if the design condition is not exactly met and provided the domain of design parameters where the principle of the device still applies. This off-optimum parameter domain is broad enough to accommodate the uncertainty in physically realizable mobilities through surface treatment of chip materials such as Polymethylmethacrylate (PMMA) and Polycarbonate (PC). Numerical

simulations have also been run to validate this theoretical outcome. In order to establish practical feasibility of the electrophoretron-based thermal cycling chip, surface modification experiments have been conducted to demonstrate that the desired sign-reversal of the electroosmotic mobility is possible for the materials of interest and to quantify the maximum magnitude of this reversed mobility.

Chapter 2 Background

When brought into contact with an aqueous (polar) medium, most substances will acquire a surface electric charge. Some of the charging mechanisms include ionization, ion adsorption and ion dissolution. The effect of any charged surface in an electrolyte solution will be to influence the distribution of nearby ions in the solution. Ions of opposite charge of that of the surface are attracted toward the surface while of like charge are repelled from the surface. This attraction and repulsion combined with the mixing tendency resulting from the random thermal motion of the ions leads to the formation of an electric double layer. In this layer, there is an excess of counterions over coions to neutralize the surface charge, and these ions are distributed in a diffuse manner.

The length-scale of this Debye layer has been estimated, for an aqueous solution at $25^0 C$ to be equal:

$\lambda_D = \frac{9.61.10^{-9}}{\left(z\ c\right)^{1/2}}$ C being the concentration of the solution and Z, the valency.

This value lies between 1 and $10\,nm$. In a channel of $50\,\mu m$-cross section the assumption of electrical neutrality is justified knowing that the one 'non-neutral' region is confined to a layer only few nanometers wide. This result is going to be useful for future discussion.

The discovery of electrokinetic phenomena may be credited to F.F Reuss who first experimented with "electroosmosis" and "electrophoresis" in 1809. He demonstrated that under the influence of an electric field water migrated through porous clay diaphragms toward the cathode. This is understood today as a demonstration of

‘electroosmotic phenomena’. In fact, as the surface is negatively charged (mineral particles in contact with small salt particles in water) the positive ions will therefore predominate in the Debye layer next to the charged surface, so application of an external field results in a net migration toward the cathode of ions in the surface water layer. Due to viscous drag, the rest of the particles of the solution are drawn by the coions and therefore flow towards the cathode.

Let us now estimate the electroosmotic velocity produced in a fine circular capillary by a uniform electric field applied across a one-dimensional channel. If the surface is assumed to be negatively charged, then the flow will be in the direction of the cathode with the electric body force per unit volume given by:

$$f_E = \rho_E \vec{E} \tag{2.1}$$

The momentum equation may be written

$$\rho \frac{D\vec{u}}{Dt} = \mu \vec{\nabla}^2 \vec{u} - \vec{\nabla} p + \rho \, \vec{g} + \rho_E \vec{E} \tag{2.2}$$

Neglecting gravitational forces and supposing the flow to be an inertia free capillary flow, with no pressure gradient the above equation simply reduces to a balance between viscous and electrical forces

$$\mu \vec{\nabla}^2 \vec{u} = -\rho_E \vec{E} \tag{2.3}$$

If, in addition the diffuse layer (Debye layer) thickness is small compared to the tube radius a , then the previous form of the momentum equation could be reduced to the one-dimensional form appropriate to a long plane channel

$$\mu \frac{\partial^2 u}{\partial y^2} = -\rho_E E_x = \varepsilon \frac{\partial^2 \phi}{\partial y^2} E_x \tag{2.4}$$

r is the Cartesian coordinate normal to x with origin at the lower channel wall and directed into the flow. The component of the electric field E_x is parallel to the surface in the positive x direction. Poisson's equation has been used to eliminate the charge density ρ_E.

At the edge of the diffuse layer, we make the assumption that

$$\frac{\partial u}{\partial r} = 0 \qquad \frac{\partial \phi}{\partial r} = 0 \tag{2.5}$$

Moreover, for $u = 0$, we set $\phi = \varsigma$ (the zeta potential)

We find that, after integration

$$u = -\frac{\varepsilon \, \zeta \, E_x}{\mu} \tag{2.6}$$

This formula for the electroosmotic velocity is known as the Helmholtz-Smoluchowski equation. Within this picture where the double layer thickness is very small compared with the geometrical characteristic length, the fluid moves as in plug flow. The velocity "Slips" at the wall, meaning that it goes from 0 to U discontinuously.

This was just to get an idea about the velocity profile induced by the electrokinetic effect for an applied voltage across a one-dimensional channel with no pressure gradient. We shall next allow for the pressure gradient, but the mean velocity and the tube radius are assumed small enough for inertia effects to be considered negligible. The electrolyte solution is supposed to be dilute and binary, i.e. has one positive ion and one negative ion.

Under this assumption, the momentum equation reduces to

$$-\vec{\nabla}p+\mu\vec{\nabla}^2\vec{u}-F(z_+c_++z_-c_-)\vec{\nabla}\phi=0 \qquad (2.7)$$

Where we have substituted

$$\vec{E}=-\vec{\nabla}\phi \qquad (2.8)$$

and

$$\rho_E=F\,\Sigma z_ic_i \qquad (2.9)$$

We assume that for the ions composing the buffer solution

$$z_+=-z_- \qquad (2.10)$$

For the axially symmetric circular capillary, we adopt a cylindrical coordinate system (x,r) with x positive in the direction of the flow and r the radial coordinate with origin at the axis of symmetry

$$\frac{\mu}{r}\frac{\partial}{\partial r}\left(r\frac{\partial u}{\partial r}\right)=\frac{\partial P}{\partial x}+Fz\left(c_+-c_-\right)\frac{\partial\phi}{\partial x} \qquad (2.11)$$

Poisson's equation provides us with

$$\nabla^2\phi=-\frac{\rho_E}{\varepsilon} \qquad (2.12)$$

Neglecting the second derivative with respect to x of the electrical potential because we assume that the length of the channel is large compared to its cross sectional radius a, we get

$$\frac{1}{r}\frac{\partial}{\partial r}\left(r\frac{\partial\phi}{\partial r}\right)=-\frac{Fz}{\varepsilon}\left(c_+-c_-\right) \qquad (2.13)$$

Because ϕ is both dependant upon x and r, then it is convenient to divide the potential into two parts

$$\phi(x,r)=\Phi(x)+\psi(x,r) \qquad (2.14)$$

Poisson's equation looks now like

$$\frac{1}{r}.\frac{\partial}{\partial r}.\left(r.\frac{\partial \psi}{\partial r}\right) = -\frac{F.z}{\varepsilon}.(c_+ - c_-) \tag{2.15}$$

Since there is no radial flow, we can assume a Boltzmann distribution for the ions in the electrolyte and then state that

$$c_{\pm}(x,r) = c_0(x).\exp(\mp\frac{zF\psi}{RT}) \tag{2.16}$$

Here, we have set $c_+^0 = c_-^0 \approx c_0$. Let us consider the following dimensionless parameters to rewrite the governing equation for ψ.

$$\begin{aligned} r^* &= \frac{r}{a} \\ \lambda^* &= \frac{\lambda_D}{a} \\ \psi^* &= \frac{zF\psi}{RT} \end{aligned} \tag{2.17}$$

We then have

$$\lambda^{*2}\frac{1}{r^*}\frac{\partial}{\partial r^*}\left(r^*\frac{\partial \psi^*}{\partial r^*}\right) = \sinh\psi^* \tag{2.18}$$

The symmetry of the problem imposes that

$$\frac{\partial \psi^*}{\partial r^*} = 0 \text{ at } r^* = 0 \tag{2.19}$$

And

$$\psi^* = \psi_w^* = \zeta^* \text{ at } r^* = 1 \tag{2.20}$$

This problem is not straightforward analytically, but numerical solutions exist.

To obtain the velocity distribution and volume rate, we can eliminate $F.z.(c_+ - c_-)$ between the Poisson equation and the momentum equation to give

$$\frac{\mu}{r}\frac{\partial}{\partial r}\left(r\frac{\partial u}{\partial r}\right)=-\frac{\varepsilon}{r}\frac{\partial}{\partial r}\left(r\frac{\partial \psi}{\partial r}\right)\frac{d\Phi}{dx}+\frac{dp}{dx} \tag{2.21}$$

The boundary conditions of the problem are

$$\begin{aligned}&\frac{\partial u}{\partial r}=0\\ &\frac{\partial \psi}{\partial r}=0\end{aligned}\quad \text{at}\quad r=0 \tag{2.22}$$

$$\begin{aligned}&u=0\\ &\psi=\varsigma\end{aligned}\quad \text{at}\quad r=a \tag{2.23}$$

Using these conditions to integrate the momentum equation gives the velocity expression

$$u(r)=-\frac{\varepsilon(\psi-\varsigma)}{\mu}\frac{d\Phi}{dx}+\frac{r^2-a^2}{4\mu}\frac{dp}{dx} \tag{2.24}$$

After integrating the velocity across the cross section, we get the expression for the flow rate

$$Q=-\int_0^a \frac{\varepsilon(\psi-\varsigma)}{\mu}\frac{d\Phi}{dx}2\pi r dr-\frac{\pi a^4}{8\mu}\frac{dp}{dx} \tag{2.25}$$

These expressions of velocity and flow rate are still not useful as ψ is still not explicitly known. From Poisson's equation we have

$$\frac{\partial^2 \psi^*}{\partial r^{*2}}=\sinh\psi^* \tag{2.26}$$

With

$$r^*=r/\lambda_D \tag{2.27}$$

With the Debye-Huckel linearization approximation, the solution for ψ is

$$\psi=\varsigma e^{-(a-r)/\lambda_D} \tag{2.28}$$

After substituting this result into the general expression for velocity and volume flow rate, we obtain

$$u = \frac{\varepsilon\varsigma}{\mu}\left(1 - e^{-(a-r)/\lambda_D}\right)\frac{d\Phi}{dx} + \frac{r^2 - a^2}{4\mu}\frac{dp}{dx}$$
$$Q = \frac{\varepsilon.\varsigma}{\mu}\frac{d\Phi}{dx}\pi a^2\left(1 - 2\frac{\lambda_D}{a}\right) - \frac{\pi a^4}{8\mu}\frac{dp}{dx} \qquad (2.29)$$

For a thin diffuse layer, that is for when $a/\lambda_D \to \infty$, the expressions for velocity and flow rate reduce to

$$u = \mu_e\frac{d\Phi}{dx} + \frac{r^2 - a^2}{4\mu}\frac{dp}{dx}$$
$$Q = \mu_e\frac{d\Phi}{dx}\pi a^2 - \frac{\pi a^4}{8\mu}\frac{dp}{dx} \qquad (2.30)$$

with

$\mu_e = \frac{\varepsilon\varsigma}{\mu}$ is the electroosmotic mobility of the surface exposed to the electrolyte.

Consider now a channel loop where we modified the chemical properties of a portion of its length. In addition, let us define the following variables and parameter L_1 : Length of the unmodified portion of the channel

L_2 : Length of the modified portion of the channel

μ_{e_1} : Electroosmotic mobility of the unmodified portion of the channel

μ_{e_2} : Electroosmotic mobility of the modified portion of the channel

Δp : Hydrodynamic pressure drop

$\Delta\Phi$: Electrical potential difference applied at the electrodes.

u_1 : Velocity in channel 1

u_2 : Velocity in channel 2

The previously presented analysis is based on the solution for combined electrokinetic and pressure-driven fully developed flow based on an assumed Boltzmann distribution for the ions in the diffuse layer, the Debye-Huckel linear approximation, circular cross section and for thin double layer. These assumptions are generally valid for the conditions of interest to the thermal cycling reactor application and give a very good approximation of the actual flow when applied in some regions of the device. Therefore, we can use the velocity and flow rate expressions that we obtained to describe the flow in the loop, in those particular zones that satisfy our assumptions. Therefore, we can state that

$$u_1 = \frac{\Delta\Phi}{\mathrm{L}_1}\mu_{e_1} - \frac{a^2}{4\mu}\frac{\Delta p}{L_1}\left(1-\left(\frac{r}{a}\right)^2\right) \tag{2.31}$$

And similarly

$$u_2 = \frac{\Delta\Phi}{\mathrm{L}_2}\mu_{e_2} - \frac{a^2}{4\mu}\frac{\Delta p}{L_2}\left(1-\left(\frac{r}{a}\right)^2\right) \tag{2.32}$$

In order to achieve cyclic motion the volumetric fluxes of the fluid must be equal and opposite in sign. Applying this condition, we obtain a relationship between the induced hydrodynamic pressure drop and the applied voltage

$$\Delta p = \frac{8\mu}{a^2}\Delta\Phi\frac{\frac{\mu_{e_1}}{L_1}+\frac{\mu_{e_2}}{L_2}}{\frac{1}{L_1}+\frac{1}{L_2}} \tag{2.33}$$

Therefore, we can now write the velocity as the function of only lengths and mobilities.

$$u_1(r) = \frac{\Delta\Phi}{L_1}\left\{\mu_{e_1} - 2\frac{\frac{\mu_{e_1}}{L_1} + \frac{\mu_{e_2}}{L_2}}{\frac{1}{L_1} + \frac{1}{L_2}}\left[1 - \left(\frac{r}{a}\right)^2\right]\right\} \tag{2.34}$$

$$u_2(r) = \frac{\Delta\Phi}{L_2}\left\{\mu_{e_2} - 2\frac{\frac{\mu_{e_1}}{L_1} + \frac{\mu_{e_2}}{L_2}}{\frac{1}{L_1} + \frac{1}{L_2}}\left[1 - \left(\frac{r}{a}\right)^2\right]\right\} \tag{2.35}$$

For an optimum design of the modified-electrophoretron, we need to respect certain criteria. An optimum design is one that achieves:

(a) Unidirectional flow of opposite sign in the two branches of different mobility. This is necessary to secure continuous cyclic flow without reversals

(b) Highly uniform velocity distribution across the channel loop throughout its length

(c) The absolute value of the electrophoretic mobility of the species should be sufficiently smaller than the absolute value of the electroosmotic mobility of the branch that has a different mobility sign

The requirement of unidirectional flow in both branches can only be satisfied if the effective mobilities in the two channels are of opposite sign, i.e. $\frac{\mu_{e2}}{\mu_{e1}} < 0$

In addition, the following condition needs to be satisfied

$$\left|\frac{\mu_{e2}}{\mu_{e1}}\right| < 2\frac{L_2/L_1}{1 - L_2/L_1} \text{ If } \frac{L_2}{L_1} < 1$$

This condition provides a window of operation in terms of the two essential parameters, effective mobility ratio and channel branch length ratio, within which unidirectional flow

is achieved everywhere in the channel loop with a finite pressure difference existing between the electrodes. Furthermore, when the length and mobilities ratios are judiciously chosen and satisfy the following relationship

$$\left|\frac{\mu_{e_1}}{\mu_{e_2}}\right| = \frac{L_1}{L_2} \tag{2.36}$$

The pressure drop is equal to zero and the velocity in both portions of the channel will be indeed distributed uniformly throughout the cross-section. This is the condition of optimal operation because it eliminates sample dispersion due to velocity non-uniformity. It is important to underline the fact that the dispersion of the sample is totally acceptable taking into the consideration the type of application for which the device is designed. In practice, this is not an absolute requirement, because the performance of the cycler is also acceptable when small non-uniformities of the velocity are present. This has been proven with numerical simulations, where off-optimum cases have been run (with opposite-sign mobilities but not-matching ratios), and the results confirmed the expectations. Figure 2.1 shows the window of operation in terms of the two essential parameters, $\left|\frac{\mu_{e2}}{\mu_{e1}}\right|$ (effective mobility ratio) and, $\frac{L_2}{L_1}$ (channel branch length ratio), within which unidirectional flow is achieved everywhere in the channel loop with a finite pressure difference existing between the electrodes

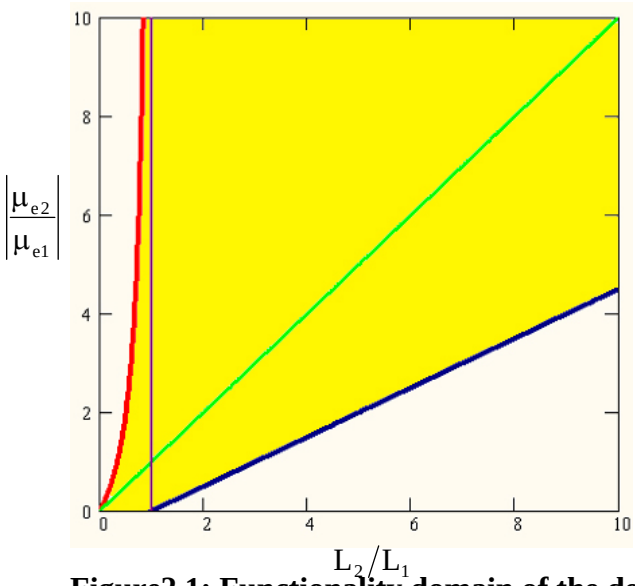

Figure2.1: Functionality domain of the device

Chapter3 Numerical Simulations

The previous chapter was about presenting an analytical solution of the problem using a particular set of assumptions. This set of assumptions led to a primary solution of the flow field in the channel that is ready to use for the only purpose of having a first idea of what is going on in the loop. This solution has also been useful for predicting an optimized configuration of the flow. However, it is important to point out the fact that the effectiveness of this theoretical analysis is limited for several reasons:

1-We assumed, for this first analysis, that the channel has a circular cross-section whereas the actual loop would have a rectangular cross section.

2-The analysis did not take into consideration the presence of electrodes. The simple fact of having them in the loop introduces a singularity that fails the analytical solution.

3-In the actual chip, there are zones located at the boundary of two different mobility regions, this has not been taken into consideration into the formulation of the analytical solution.

4- It assumes that the channel is straight with a uniform cross-section. This assumption is not respected in the actual chip because of the presence of bends and corners.

For all the reasons above, simulations are necessary to find out about the flow profile in every cross-section of the loop, because the actual geometry does not satisfy the analytical solution set of assumptions. However, we expect the qualitative flow behavior in the straight parts of the channels to tend to that we got using the theoretical analysis in the straight parts of the loop, in regions far from the electrodes and corners influence.

3.1 Problem Set Up

The basic equations describing the fluid motion are the Navier-Stokes equations with appropriate electro migratory flux terms to represent the effect of applied electric field on the carrier and/or the charged species. The applied electric field can interact with the fluid and charged species in many ways. Coventorware has been used as the solver to simulate the combination of three major phenomena: electrophoresis, electroosmosis, and hydrodynamic flow

3.1.1 Formulation

- **Electrophoresis**

The basis for electrophoresis is the differential migration of the charged species ions relative to the carrier molecules under the application of the external field. The differential migration is primarily an effect of the difference in the net charge between the solvent and solute ions, although frictional effects also have some relevance. The migration velocity of the charged species can be expressed in terms of the applied field strength as

$$\vec{u}_{ep} = \mu_{ep}\vec{E} \quad (3.1)$$

where μ_{ep} is the electrophoretic mobility of the ion in the carrier species.

Basically when a species has an electrophoretic mobility μ_{ep} and is put under an electrical field of strength $\vec{E}$, it moves under the effect of an electrical body force with a speed $\vec{u}_{ep}$.

- **Electroosmosis**

The physical aspects of electroosmosis, was discussed in the previous chapter. The determination of the electroosmotic flow field requires the solution of the Navier-Stokes

equation. Incorporating the electroosmotic effect as a body force. The governing equations for an incompressible flow become

$$\vec{\nabla} \cdot \vec{u}_{eo} = 0 \text{ (Continuity)} \qquad (3.2)$$

$$\frac{D(\rho \vec{u}_{eo})}{Dt} = -\vec{\nabla} p + \vec{\nabla} \cdot \left(\mu \vec{\nabla} \vec{u}_{eo}\right) + \rho_e \vec{E}\,, \qquad (3.3)$$

where $\vec{u}_{eo}$ is the induced electroosmotic velocity, D/Dt is the material derivative, μ is the fluid dynamic viscosity, and p is the pressure. The last term in the momentum equation represents the electrical force on the fluid particle.

Here ρ_e is the charge density and E is the electric field intensity. The electric field can be expressed in terms of a potential the divergence of which is related to the charge density, leading to

$$\begin{aligned} \vec{E} &= -\vec{\nabla}\Phi \\ \vec{\nabla}^2\Phi &= -(\rho_e / \varepsilon) \end{aligned} \qquad (3.4)$$

The electric potential Φ can be further decomposed into two components, ϕ, the externally applied potential and ζ, the zeta potential at the walls

$$\Phi = \phi + \zeta \qquad (3.5)$$

Under the assumption that the zeta potential effects are confined to a very small region near the wall, the charge distribution is assumed to be governed by the zeta potential alone, independent of the external field. This allows the decomposition below

$$\begin{aligned} \vec{\nabla}^2\phi &= 0 \\ \vec{\nabla}^2\zeta &= -\left(\rho_e / \varepsilon\right) \end{aligned} \qquad (3.6)$$

The equation for the zeta potential can be simplified by the Debye-Huckel treatment for the charge density. This is based on the concept of a diffuse double layer, which assumes that the double layer extends for some finite distance into the fluid. Through the Debye-Huckel approximation the charge density on the walls can be determined through the Boltzmann equation and results in the Poisson-Boltzmann equation for the zeta potential:

$$\nabla^2\zeta = \frac{2n_0 ze}{\varepsilon\varepsilon_0}.\sinh\left(\frac{ze}{kT}\zeta\right) \qquad (3.7)$$

Where n_0 is the ionic concentration, z is the valence of the charged buffer, e is the electron charge, k is the Boltzmann constant and T is the temperature. ε_0 is the permittivity of vacuum .

Assuming that $ze << kT$, the previous equation reduces to

$$\nabla^2\zeta = K^2\zeta \qquad (3.8)$$

Where

$$K = \left(2n_0 z^2 e^2 \Big/ \varepsilon\varepsilon_0 kT\right)^{\frac{1}{2}} \qquad (3.9)$$

K is the Debye-Huckel parameter, and $1/K$ is termed as the characteristic thickness of the double layer.

In water-based systems, this thickness is small enough to allow the following representation for purely electroosmotic flow

$$\vec{u}_{eo} = \mu_{eo}\vec{E}\,, \qquad (3.10)$$

where μ_{eo} is the electroosmotic mobility, which relates the fluid velocity at the wall to the electric field. This approach is valid as long as the thickness of the EDL is less than few fractions of a percent of the characteristic geometrical length scale of the flow domain.

The electroosmotic mobility can be determined either experimentally or as a function of more fundamental quantities. By balancing the electrokinetic force with viscous forces, an analytical solution of the two-dimensional Navier-Stockes equations yields an expression for the electroosmotic mobility as a function of the zeta potential

$$\mu_{eo} = \frac{\varepsilon\varepsilon_0\zeta}{\mu} \qquad (3.11)$$

Where μ is the dynamic fluid viscosity.

The motion of a charged species in the electric field can be determined by coupling the species transport equation with the above equations through a net convective velocity.

$$\frac{\partial c_i}{\partial t} + (\vec{u}_{eo} + \vec{u}_{ep}) \cdot \vec{\nabla} c_i = D\vec{\nabla}^2 c_i \qquad (3.12)$$

3.1.2 Assumptions and Hypotheses

In this section, we list all the assumptions used in the formulation.

-We assume that the buffer solution is neutral everywhere in the channel except for the Electrical Double Layer.

-We assume that the concentration of ions in the sheath has a Boltzmann distribution.

-We consider the so-called Debye-Huckel approximation that allows solving for the zeta potential.

- We neglect gravitational forces -We assume that the diffuse layer thickness is very small relatively to the channel dimensions (width, depth and a fortiori length)

Table3.1: Cases Summary

Equation 1 Case	Electrophoretic Mobility of species μ_{ep} ($\mu m^2/(V\,s)$)	Electroosmotic Mobility Branch 1 μ_{e_1} ($\mu m^2/(V\,s)$)	Electroosmotic Mobility Branch 2 μ_{e_2} ($\mu m^2/(V\,s)$)	Electroosmotic Mobility to Electrophoretic Mobility Ratio	Relationship between Mobility and Length ratios
1	$-3.75\ 10^4$	$7.1\ 10^4$	$-2.56\ 10^4$	$\left\|\frac{\mu_{e_1}}{\mu_{ep}}\right\| \approx 1.89$	$\left\|\frac{\mu_{e_1}}{\mu_{e_2}}\right\| = \frac{L_1}{L_2} \approx 2.77$
2	$-3.75\ 10^4$	$5.68\ 10^4$	$-1.372\ 10^4$	$\left\|\frac{\mu_{e_1}}{\mu_{ep}}\right\| \approx 1.51$	$\left\|\frac{\mu_{e_1}}{\mu_{e_2}}\right\| = 1.5\frac{L_1}{L_2} = 4.16$
3	$-3.75\ 10^4$	$7.1\ 10^4$	$-1.7\ 10^4$	$\left\|\frac{\mu_{e_1}}{\mu_{ep}}\right\| \approx 1.89$	$\left\|\frac{\mu_{e_1}}{\mu_{e_2}}\right\| = 1.5\frac{L_1}{L_2} = 4.16$
4	$-3.75\ 10^4$	$7.1\ 10^4$	$-5.1\ 10^4$	$\left\|\frac{\mu_{e_1}}{\mu_{ep}}\right\| \approx 1.89$	$\left\|\frac{\mu_{e_1}}{\mu_{e_2}}\right\| = 0.5\frac{L_1}{L_2} = 1.385$

-The electrolyte solution (buffer) is taken to be dilute and binary. When the dilute assumption is set, the species concentration is modeled as having no influence on the electrical conductivity and therefore does not influence the electrical field.

3.1.3. List of Cases:

In order to provide proof of concept for the modified micro-scale electrophoretron, we needed to test it via simulations for several configurations and make sure to consider situations where the design is not optimized in order to prove the wide domain of functionality of the device. Table 3.1 summarizes the four cases for which simulations have been run.

The first case examines the extent to which the optimum configuration predicted by the simple theory for channels of circular cross-section is valid for the more realistic closed

loop channel with a rectangular cross-section including bends and electrodes. In this case, the ratio of lengths of the two branches of the loop match exactly with the ratio of the electroosmotic mobilities of those two branches. In addition, the second condition requiring $\left|\mu_{e_1}\right| > \left|\mu_{eph}\right|$ is also satisfied. The theoretical analysis presented in the previous chapter indicates that when this condition is met, the pressure gradient through the branches of the loop should tend to zero and the hydrodynamic diffusion and distortion of the species plug ought to be minimized. Minimizing the pressure gradient in the loop is beneficial in terms of managing leaks. In fact, the final design of the modified micro scale electrophoretron will contain several access channels that are attached to the loop, those extra channels will serve the purpose of degasification to prevent bubble formation or would link the reservoirs that accommodate the electrodes to the loop in case we choose to not put them on the top surfaces of the channel as simulated in our cases or might also serve to load the plug to the loop. We know, thus, for fact that our loop is prone to have a lot of openings that would lead to consequential leaks. It is mathematically proven that the larger the pressure gradient is in the micro channel the longer those access channels would have to be in order to achieve a certain percentage of leakage. In order to have a reasonable access channel length for certain leakage rate, we need to have a relatively low pressure gradient. Cases 2 and 3 are examples of off-optimum configurations where the first condition of mobility/length ratios is not met. In fig2.1 those two cases are located above the line (green) that represents the optimum configuration case. Case 4 is off optimum as well and is illustrating a case that could be located below the optimum case line in fig2.1. One can argue that both cases 2 and 3 are proving the same point, it is important to draw the reader's attention to the third condition

of functionality of the device that is dependant upon the contrast in terms of absolute value between the electroosmotic mobility and the electrophoretic mobility of the species in the branch where they are of opposite sign. For the device to work properly, we need $\left|\mu_{e_1}\right| - \left|\mu_{eph}\right|$ to be important enough for the species to be dragged by the electroosmotic flow to the electrode of interest. In case 3 this difference is larger than in case 2.

3.1.4 Simulations Set Up

Now that we know what would be the proportion of the channel's branches, we need to know the total length so that we can design the geometry and start working on the numerical simulations. Initially the total length of my loop was 76mm. This length required a substantial computational effort and memory allocation considering the spatial resolution requirements of the numerical solution. Thus, we decided to switch to a smaller geometry with the same proportions of channel-branch lengths that would illustrate the principle of design without the large computational burden. The total length was picked considering the software limitations in terms of grid density and maximum number of mesh elements allowed. So, a channel with a total length of 8 mm was used. This length offered the best compromise between the software limitations and the grid density (for calculation accuracy and grid independence purposes). This length will be the one that I will use for my simulations, the presence of the electrodes, the departure from circular cross section (upon which the theory is based) and the electrode placement effects caused the velocity profile to be not as uniform and smooth as predicted. We had to remediate to that by considering some correcting strategies that I will expand in a subsequent section of this thesis.

3.1.4.1 Meshing

Considering the special features of the geometry to mesh, we had to use the best grid available to obtain the most accurate results possible. The software that we used for the simulations offered several options in terms of the geometry of the finite element that is to be used for the calculations, for example for a rectangular geometry one could use a rectangular finite element, for a triangular geometry one could use a triangular finite element and finally for a circular geometry a circular finite element is available. Because of the complex geometry of the loop, that could not be assimilated to a simple geometrical category (all-rectangular, all-circular or all-triangular), we judged that for the best calculation results in terms of accuracy , the element to choose is of a hexahedral shape. The mesh that suits our geometry the most is the *extruded bricks-pave Q-morph*. This option creates a hexahedral mesh by meshing the top layer in the X,Y direction and then extruding that mesh in the Z direction through all the layers .

Pave-Q morph option meshes arbitrarily shaped layers that are orthogonal along the selected extrude direction and then extrudes them to obtain a brick mesh of non orthogonal shapes. the tool works by imprinting the planar faces of the layers in the region , meshing this set of 2-D faces and then extruding the 2-D mesh through the rest of the layers . It creates an unstructured, quadrilateral mesh starting from the outer boundaries and moves inward in a layered fashion. Two possible kinds of such elements are available through the software used (Coventorware^{TM}) linear and parabolic. We opted for the linear ones because we could obtain faster results with them, and a test proved that the difference between those two options in terms of accuracy of the results for our problem was insignificant. A grid independence study was carried out initially for the

most grid-demanding case (e.g. one with the largest gradients) of the ones presented here. This was done so that the same grid could be used for all cases. The criterion used to arrive at the appropriate grid was based on a global error of <1% and a maximum local error of not more than 5%. Error here designates difference between two grids compared.

3.1.4.2 Boundary Conditions

In order to fully specify the problem to be solved and in addition to the governing equations presented above boundary conditions must be specified.

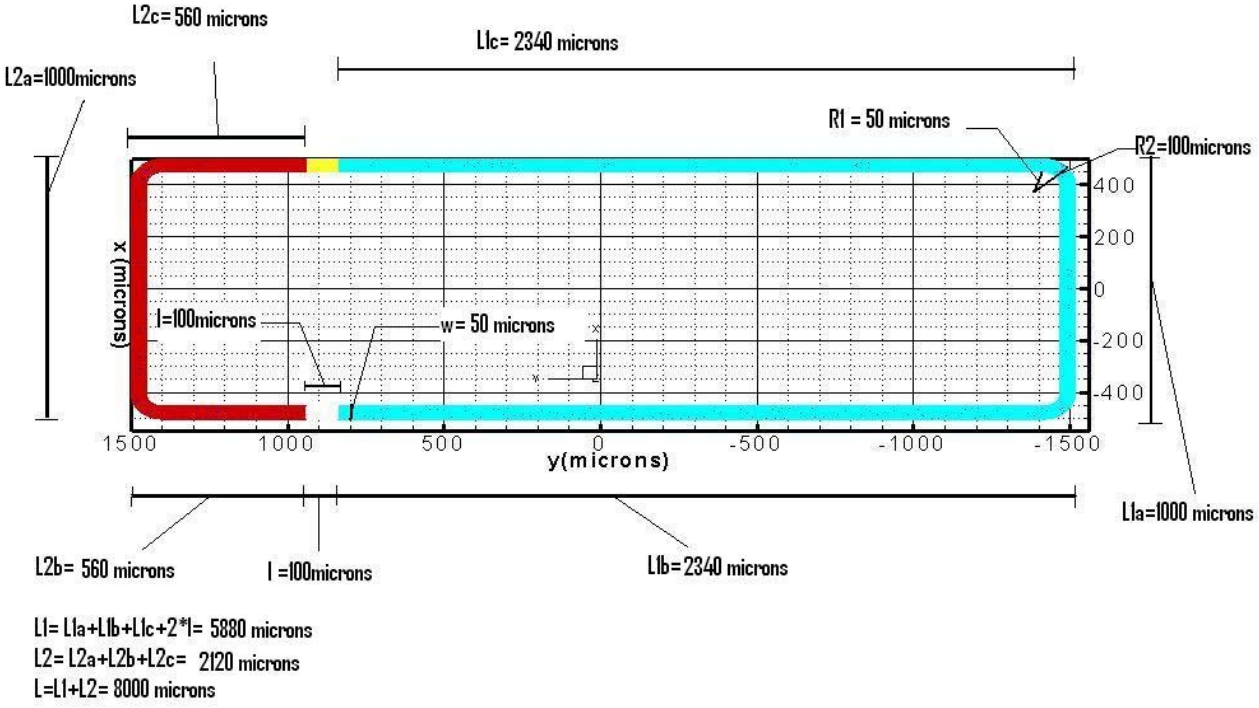

Figure3.0: Geometry of the simulated channel.

- **Voltage**

The loop contains two electrodes, necessary to create the electroosmotic flow, so we had to specify the potential on each electrode, which was modeled as an equipotential surface. We set the anode at 250V and the cathode at 0V.

- **Concentration profiles**

Conservation of mass is used to solve for the species concentration. At the walls, the following boundary condition is considered imposing a zero mass flux of the species across all rigid boundaries (walls):

$$\vec{n} \cdot \vec{\nabla} c = 0, \qquad (3.13)$$

$\vec{n}$ represents the unity vector, perpendicular to the surface of the inner walls.

- **Velocity**

The boundary condition at the walls for the velocity is:

$$\vec{u} = \mu_e \vec{E} \qquad (3.14a)$$

and $\vec{u}.\vec{n} = 0$ (3.14b)

(at every wall of the whole loop), $\vec{n}$ stands for the unity vector normal to the surface.

The first equation emphasizes the fact that for equi-potential surfaces (electrodes top surfaces) the velocity is zero, and shows the duality between the electrical field and the velocity field: hey have the same direction and their magnitudes are proportional. The second equation shows that there is no penetration at the walls (zero wall-normal velocities).

3.2 Case 1

This first case corresponds to the predicted “optimum” design. Naming this case “optimum” deserves further clarification. There are analytical and geometrical limitations that do allow for a perfect prediction of the flow in the whole channel. Meanwhile, those constraints do not prevent us from getting a very good approximation of what is actually happening in the straight part of the channel, far from the electrode zones and the bends and corners (even if the cross-section is rectangular and not circular as assumed above).

The optimum case simulation is the one where the mobility and length ratios match perfectly so that we have $\left|\frac{\mu_{e_1}}{\mu_{e_2}}\right| = \frac{L_1}{L_2}$, because for this case, the pressure gradient in the straight channel segments should theoretically nonexistent and there should be no induced hydrodynamic flow. The velocity profile should be uniform across the cross section and this alleviates the distortion of the plug that is usually induced by the velocity non-uniformity. This is done in the effort of minimizing the diffusion consequences and keeping the DNA template altogether the longest possible.

It is important to draw the reader's attention to the issues of the plug's distortion and diffusion. The only reason why it is important to minimize the plug's deformation, distortion or diffusion during its motion through the channel is that, it is vital, for the proof of concept, to have a visual effect that shows that the species does indeed make the circular motion that we want it to do. In the case of a PCR reactor for example, the simulation cases below all show, that the DNA cocktail will go through the three temperature zones that are necessary for the PCR reaction to occur. Now, if we put the visual effect motivation aside, the plug's diffusion through the channel while performing the circular motion is completely acceptable, taking into consideration the nature of applications for which the modified micro-scale electrophoretron is designed.

3.2.1 Electroosmotic Mobilities

We had to choose the mobility values that would serve the purpose of the design. In one branch of the loop, we had to consider an electroosmotic mobility to reverse the EOF, and the flow had to be towards the cathode in the remaining part of the channel

$$\mu_{e_1} = 7.1.10^4 \mu m^2 / V.s$$
$$\mu_{e_2} = -2.56.10^4 \mu m^2 / V.s$$

We assigned these values to each inner wall of the channel depending on the specific branch. We also imposed a no-penetration boundary condition at the top surface of the walls that hosted the electrodes. The no slip condition (zero velocity) is also satisfied on the surface of the electrodes since the electrical field lines are perpendicular to this surface.

The mobility values used here are feasible ones for unmodified and modified PC because this device is intended for PCR reactions and PC seems to be the best material to work with taking into consideration its glass transition temperature. It is important to note that the principle is valid no mater what the values of those parameters are as long as the conditions stated in Chapter 2 are satisfied.

3.2.2 Results

We will examine the computational results in terms of the velocity profiles and their characteristics in the various regions of the close-loop channel, the pressure distribution along the channel and above all the species profiles and its motion through the channel.

3.2.2.1 Velocity Profiles in the Straight Parts of the Channel Loop

The plane Y=0 microns is located in the right side part of channel 1, that is far from the electrodes region (zone where there is a change in the mobility sign that causes the reference analytical solution to fail) and the corners (zones where the flow is not uniform). The plane X=0 microns is located at the center of channel 2. These parts of the loop are expected to be the ones where the flow characteristics are the most similar to the

ones predicted by the analytical solution. Also, it was important to take one sample of each channel because the boundary conditions, particularly the electroosmotic mobilities, vary from channel 1 to channel 2.

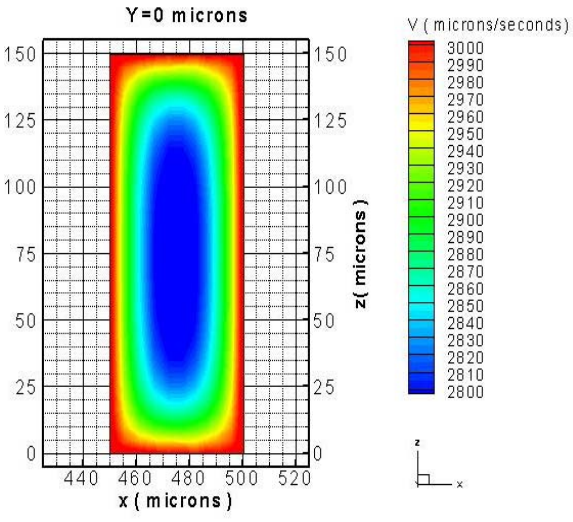

Figure3.1: Stream wise velocity ($\mu m.s^{-1}$) in the Y=0 μm plane for X>0 for case1

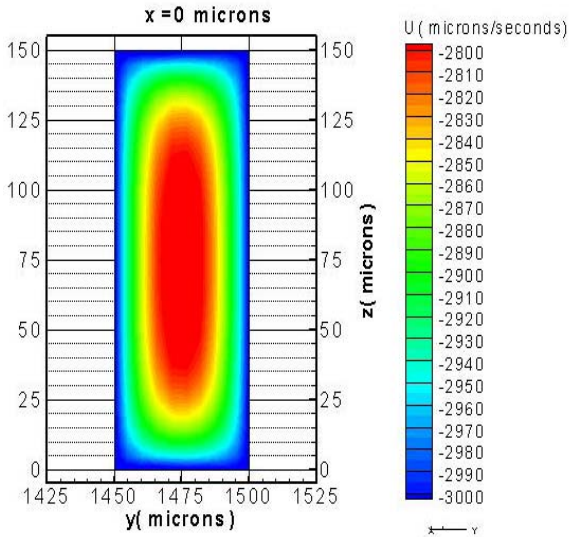

Figure3.2: Stream wise velocity ($\mu m.s^{-1}$) in the X=0 μm plane for Y>0 for case1

The velocity profile is not completely uniform throughout the channel's cross-section, there is a 10% difference in the magnitude of the velocity between the core flow and the flow right next to the walls of the channel. This is partially due to the fact that the theoretical assumptions that we used for our calculations models were completely true for circular cross-sectional channels, while our loop's cross-section is rectangular. Clearly, the theoretical analysis held in the previous chapter that predicted a quite-flat velocity profile is relevant. It is important to notice that for this first case, the velocity magnitude is the same throughout the whole loop; that is due to the fact that $\left|\frac{\mu_{e1}}{\mu_{e2}}\right| = \frac{L_1}{L_2}$, which leads

to $\frac{|\mu_{e1}|}{L_1} = \frac{|\mu_{e2}|}{L_2}$ and thus the same velocity boundary condition applies everywhere in the loop, thus the same flow profile throughout the whole loop.

The symmetry of the geometry along with the symmetry of the boundary conditions with respect to the Y axis allow us to predict a symmetrical flow profile (with the exception of the electrodes region and the corners and bends of the loop) and that is what figures 3.3 and 3.4 are about.

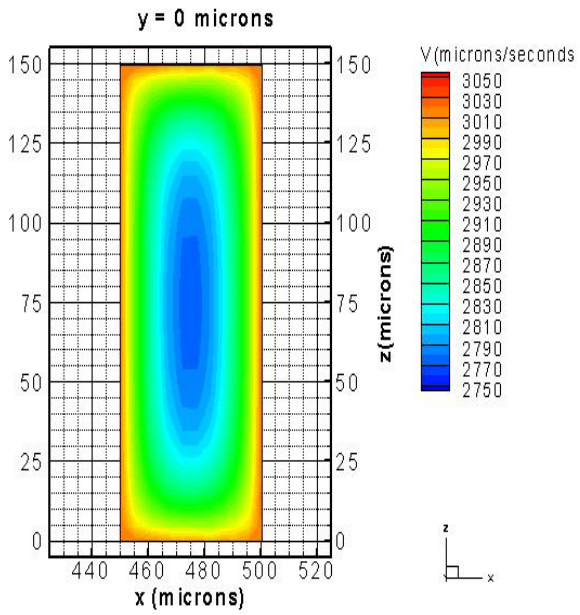

Fig3.3:Stream wise velocity ($\mu m.s^{-1}$) distribution on the Y=0 μm plane for X>0 for case 1

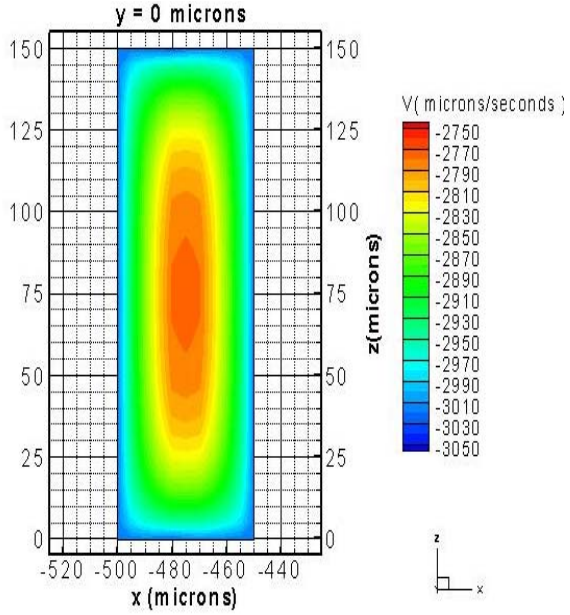

Fig3.4:Stream wise velocity ($\mu m.s^{-1}$) distribution on the Y=0 μm plane for X<0 for case 1

In Figure 3.4 we can see that the streamwise velocity goes from an approximate minimum value of 2750 $\mu m.s^{-1}$ to a maximum of 3050 $\mu m.s^{-1}$. On the opposite side of the loop with respect to the Y-axis, the velocity values go from -3050 $\mu m.s^{-1}$ to a maximum of -2750 $\mu m.s^{-1}$. The non-uniformity of the principal velocity component is approximately +/-5% of the arithmetic average of the maximum and minimum values.

After doing the same comparison for the two other cross-flow velocity components, we can state that the flow is symmetrical with respect to the Y- axis in the whole loop with the exception of the electrode region.

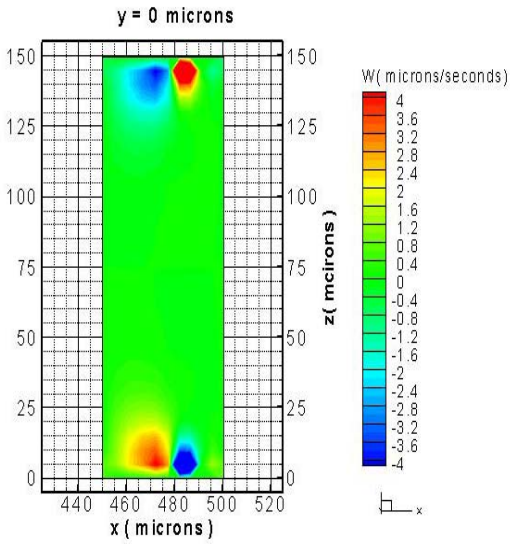

Fig3.5:Cross Flow velocity ($\mu m.s^{-1}$) distribution on the Y=0 μm plane for X>0 for case1

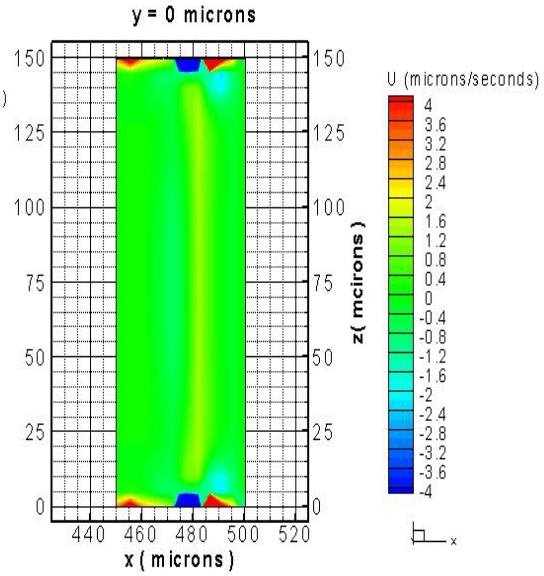

Fig3.6:Cross Flow velocity ($\mu m.s^{-1}$) distribution on the Y=0 μm plane for X>0 for case1

Figures 3.5, 3.6 and 3.3 represent the velocity components at Y=0microns for the first case “case1”, this slice is considered to represent the flow in the majority of the loop because of its location: away from electrodes location and away from bends and corners. The U velocity, which is the streamwise velocity, is larger by three orders of magnitude, than the secondary velocities, i.e. the secondary velocities are essentially negligible as expected from theory.

3.2.2.2 Species Plug Evolution

The simulated species is a plug of DNA. It has an electrophoretic mobility of

$\mu_{ep} = -3.75.10^4\,\mu m^2/V.s$. The figure sequence 3.8 through 3.16 show the progress of the DNA plug as it moves through the channel loop. The time-step between two successive figures is $0.6\,\text{sec}$. Apparently:

-The species does go through the channel in a circular motion.

-The species plug is distorted to a small extent by the weak velocity profile non-uniformity in the straight parts of the channel

-The species plug is distorted after going through the electrode-zones and the bends of the channel. The additional distortion of the plug at the bends is because of a non-uniformity of the electrical field lines caused by the fact that the inner boundary length is different than the outer boundary length. The hydrodynamic effect away from the electrodes is global and it is principally because of departure from the ideal operating condition because of the presence of the electrodes, and possibly because the proportions of the channel branches were chosen on the basis of predictions from circular channel solutions.

The electrodes are zones where the velocity field is three-dimensional and this influences the species motion and the shape of the species plug; we will explain their effect more thoroughly in a following section.

The plug becomes diluted as it goes around the loop due to diffusion and the deformations caused by the velocity profile non-uniformity and the strong three-dimensional effects in the electrode regions. In fact the species plug concentration does not decrease dramatically until it crosses the first electrode; it decreases furthermore after it crosses the second one. In addition to the convective effect of the fluid buffer additional distortion and dispersion of the plug occurs in the region near the electrodes because the

charged species are attracted by one electrode (the positive one in this case) and repelled by the other (negative in this case) and because the electrical field lines are strongly bent in the electrode region.

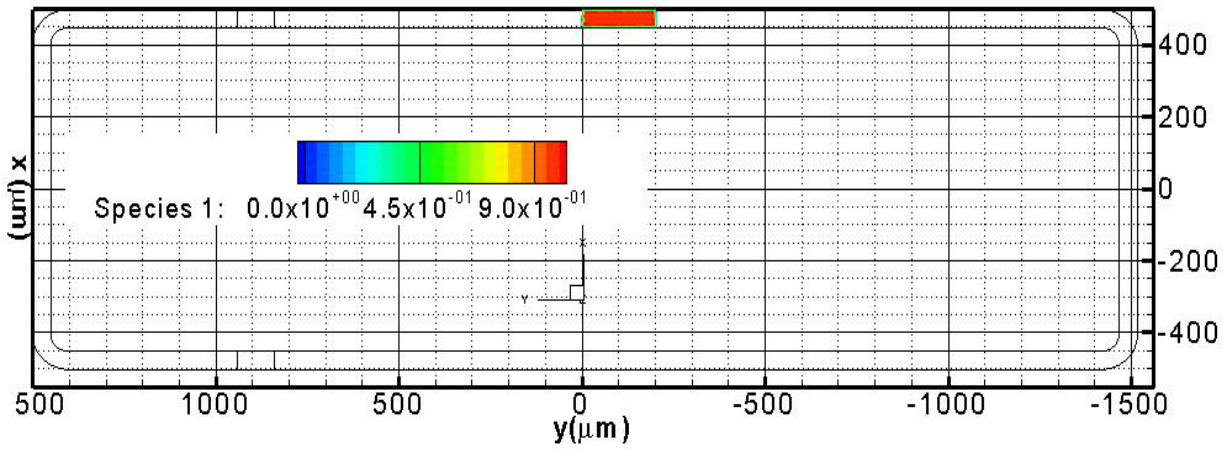

Figure3.7: Species plug at t=0sec shown on a section through the channel at Z=75 μm for case 1

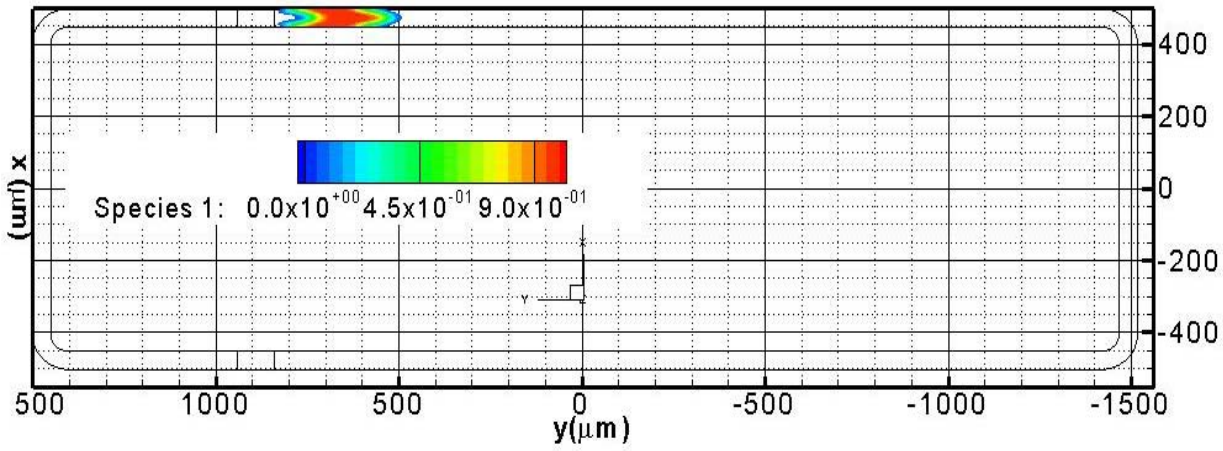

Figure3.8: Species plug at t=0.6sec shown on a section through the channel at Z=75 μm for case 1

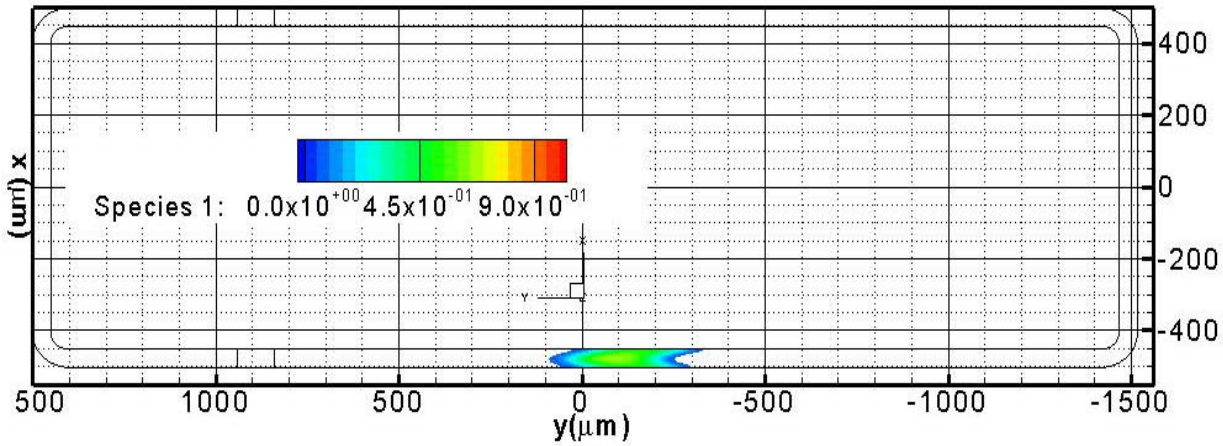

Figure3.9: Species plug at t=1.8sec shown on a section through the channel at Z=75 μm for case 1

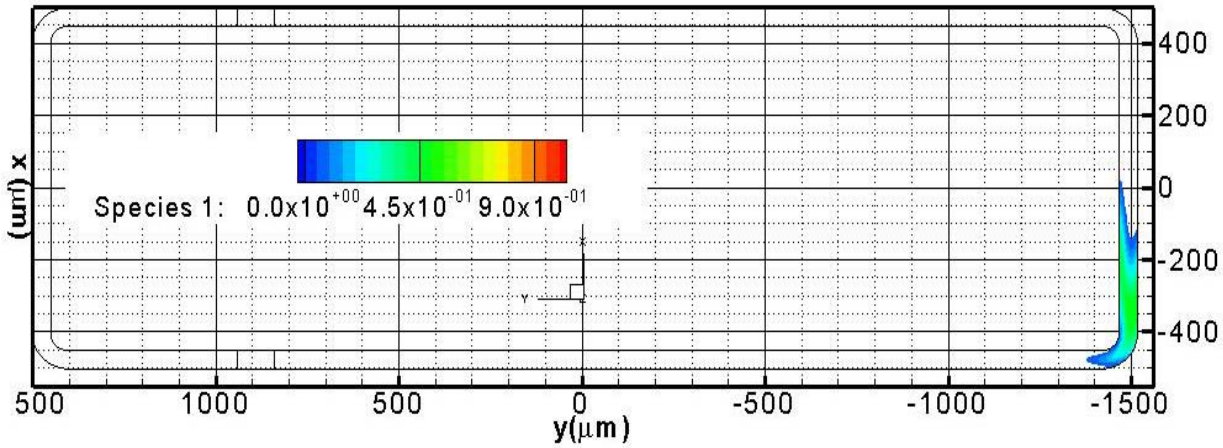

Figure3.10: Species plug at t=3.0sec shown on a section through the channel at Z=75 μm for case 1

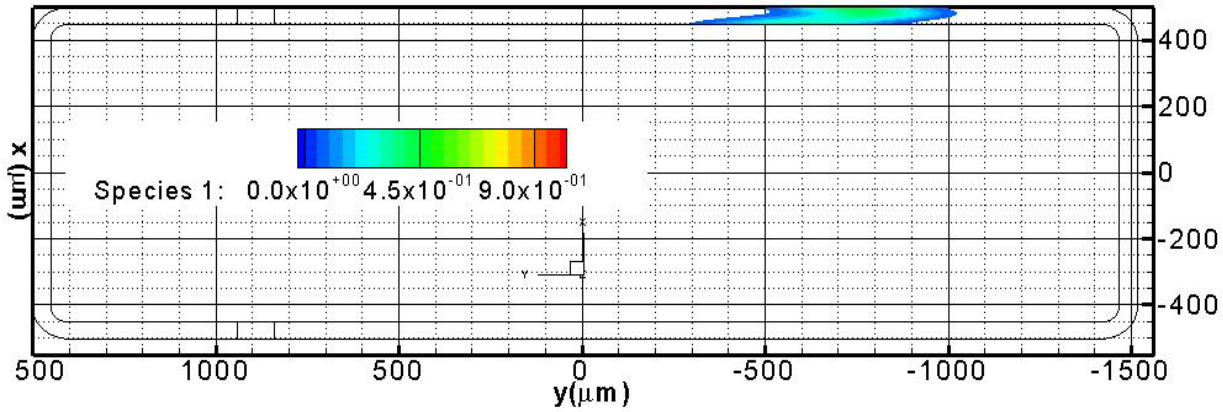

Figure3.11: Species plug at t=4.2sec shown on a section through the channel at Z=75 μm for case 1

3.3 Case2

This case is not an off-optimum one. The mobility ratio is 50% larger than the length ratio α required by the ideal condition, i.e. $\frac{\mu_{e1}}{\mu_{e_2}}$ is 1.5α. This ratio does not violate any of the theoretical rules previously stated in Chapter 1 and is within the operational window of the device (Figure2.1) .

Also for for the species to move in a the loop continuously and unidirectionally, it is important that μ_{e_1} is large enough compared to μ_{ep}. This condition is also met with the chosen values of the mobilities. In this case the contrast between μ_{e_1} and μ_{ep} is smaller than in the optimal case because μ_{e_1} is 20% smaller than what it was in the first case.

3.3.1. Electroosmotic Mobilities

The same boundary conditions are used as previously, except for the electroosmotic mobilities. To achieve the new ratio we used

$$\mu_{e_1} = 56800 \mu m^2 / V.s$$
$$\mu_{e_e} = -13720 \mu m^2 / V.s$$

These values are within the practically achievable ranges for a pristine and surface-modified material combination.

3.3.2 Results

Knowing that we are perturbing the optimum conditions, the pressure gradient is expected to be more important than in the first case which will induce a more non-uniform flow profile. It is interesting to quantify those non-uniformities.

3.3.2.1 Velocity Profiles in the Straight Parts of the Channel Loop

The velocity magnitude in this case is smaller than in case1, this is due to the fact

that the electroosmotic mobility of the first branch of the channel is smaller. Therefore, if we want to increase the magnitude of the bulk flow we need to choose materials with high electroosmotic mobilities and/or use surface modification technology to enhance the electroosmotic property of the material of interest. Also, the velocity gradient in the radial direction is larger in this case than in case1. This is due to the mismatch between the mobility /length ratios that fails the first condition for an optimum configuration. Let us now take a closer look at the velocity distributions in both channels near the wall and interpret them.

This case satisfies the following relationship:

$$\left|\frac{\mu_{e1}}{\mu_{e2}}\right| = 1.5.\frac{L_1}{L_2}$$

Which leads to $\frac{|\mu_{e1}|}{L_1} = 1.5.\frac{|\mu_{e2}|}{L_2}$ and because $u = \mu_e.\frac{\Delta\Phi}{L}$ we end up having

$u_{e1} = 1.5u_{e2}$, with u_{e1} and u_{e2} being the electroosmotic velocities immediately near the walls. So, we should expect a wall velocity in channel 1 that is roughly equal to 1.5 the velocity in channel 2, in regions far from the corners and the electrodes. In figures 3.12 and 3.13, we can see that u_{e1} is about 2500 $\mu m.s^{-1}$, while u_{e2} is about 1700 $\mu m.s^{-1}$, so that confirms our logical expectations of the velocities values next to the channel's inner walls. The non-uniformity of the principal velocity component is approximately +/-20% of the arithmetic average of the maximum and minimum values and is larger in this case than case 1.

Of course, we made sure that the flow in this case, just like the previous case is indeed unidirectional and symmetrical, by checking the channel branches and all the zones where the flow is not influenced by the electrodes presence or the corners and bends.

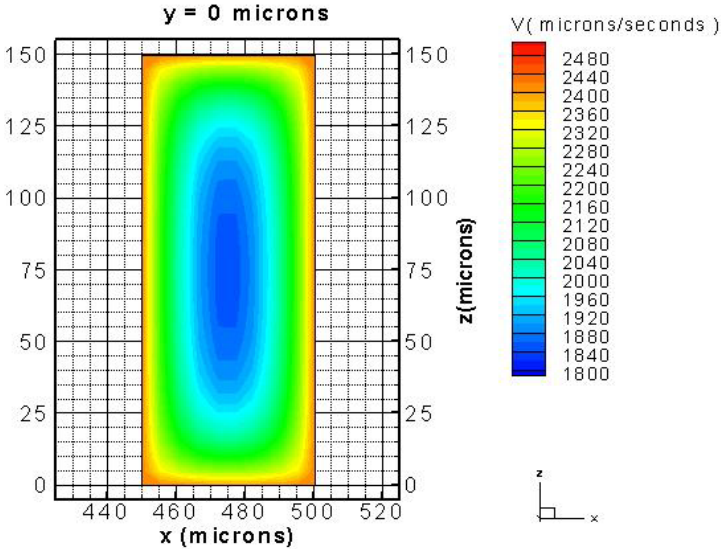

Figure3.12: Stream wise velocity ($\mu m.s^{-1}$) distribution on the Y=0 μm plane for X>0 for case2

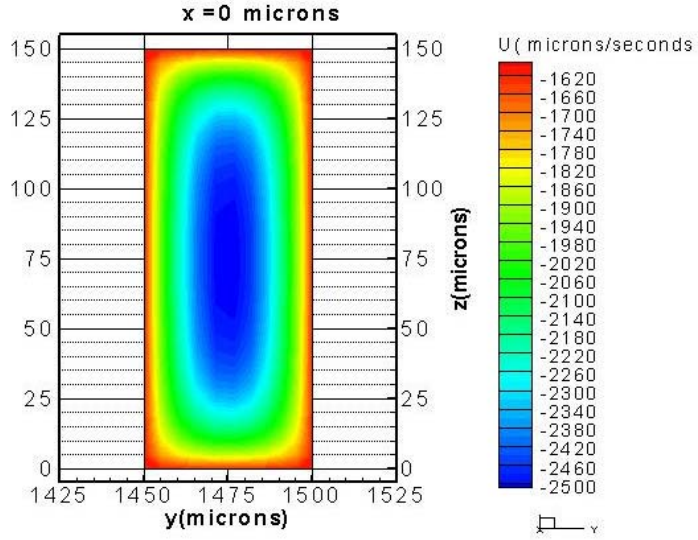

Figure3.13: Stream wise velocity ($\mu m.s^{-1}$) distribution on the X=0 μm plane for Y>0 for case2

3.3.2.2 Species Plug Evolution

The figure sequence 3.14 through 3.19 show the progress of the DNA plug as it moves through the channel loop. The time-step between two successive figures is $1.2\,\text{sec}$. The following observations are made from the species plug evolution:

-The species moves slower through the channel but still maintaining a unidirectional motion. This is due to several factors; first of all, the overall electroosmotic flow is slower compared with case1. Because the species motion is partially governed by electroosmosis, it makes the species take more time to make the loop. In addition, μ_{e_1} is smaller in this case than in case1. We may remind the reader that branch 1 is the part of the loop that has an electroosmotic mobility that is of opposite sign to the electrophoretic mobility of the species. Because in this case, μ_{e_1} is smaller than in the previous case, the electroosmotic flow is weaker and it takes more time to drag the species towards the electrode of interest. It is important to underline that the species still makes the loop because in terms of absolute values the electroosmotic mobility, μ_{e_1}, is larger than the electrophoretic mobility, μ_{eph}.

-The species plug is distorted after crossing the electrodes/corners zones. The species is heavily distorted in branch one. The species in this case is more prone to get distorted because of the stronger velocity non-uniformity relative to case 1. However, the principal cause of distortion is because of the three-dimensional flows and the bending of the electrical field lines in the electrode region and it is most visible towards the bottom of the channel (Z=10 μm**,** Figure 3.14bis). This is also true for case 1 although not shown in the associated figure sequence (Figures 3.7 to 3.11) where the species concentration profiles are given at mid-plane (Z=75 μm)

-The presence of the bends in the channel also contributes to distorting the shape of the species plug as seen in Figures 3.17 to 3.19. Since the bends are always to the left there is a compound effect as the plug goes around the loop.

-The species plug distortion occurring in channel 2 is rectified to a great extent when the species goes through the second electrode because the three-dimensional secondary flows in this region are reverse relative to those in the opposite electrode and the electrical field lines are also bent in the opposite direction.

-The diffusive dilution of the plug is enhanced because of the distortion experienced in channel 2.

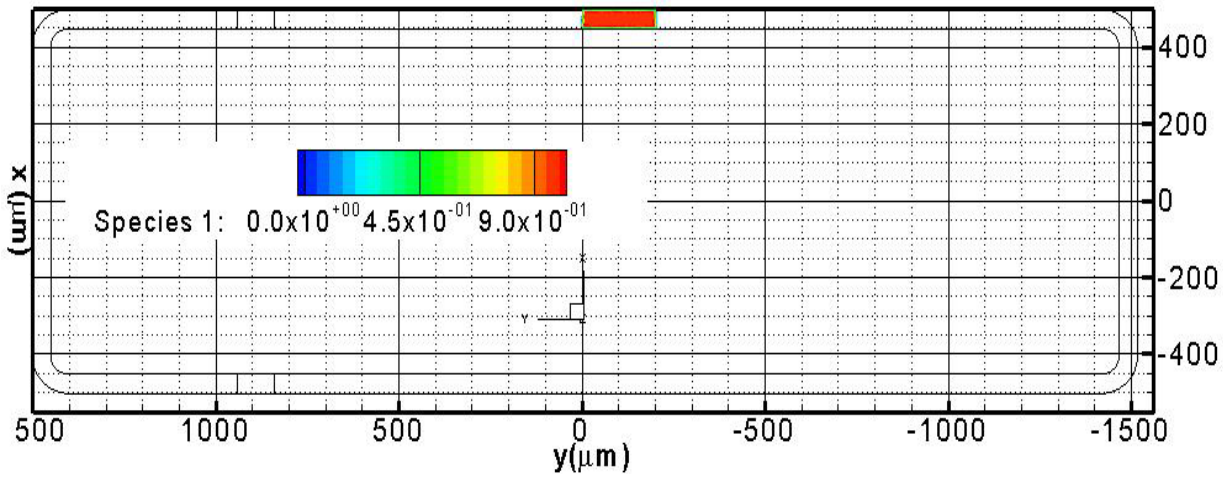

Figure3.14: Species plug at t=0sec shown on a section through the channel at Z=75 μm for case 2

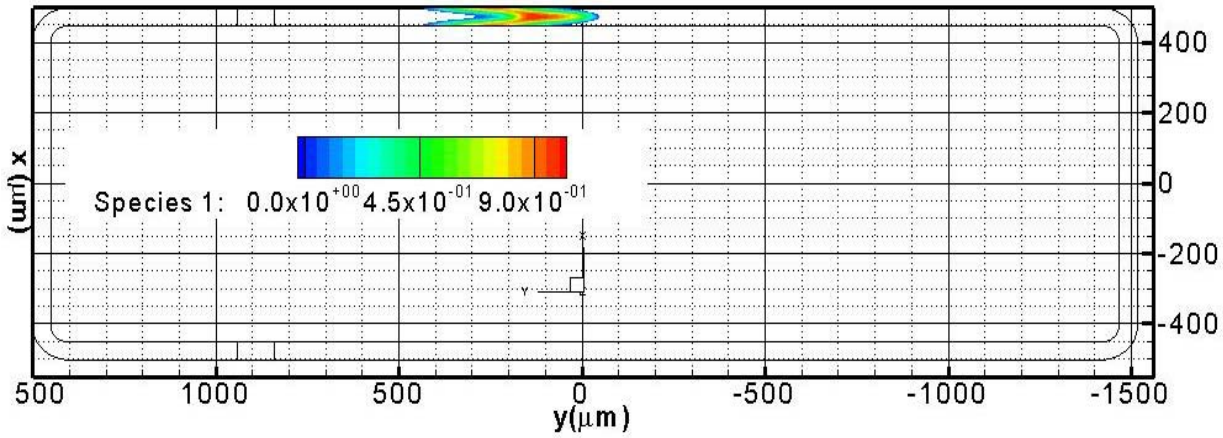

Figure3.15: Species plug at t=0.6sec shown on a section through the channel at Z=10 μm for case 2

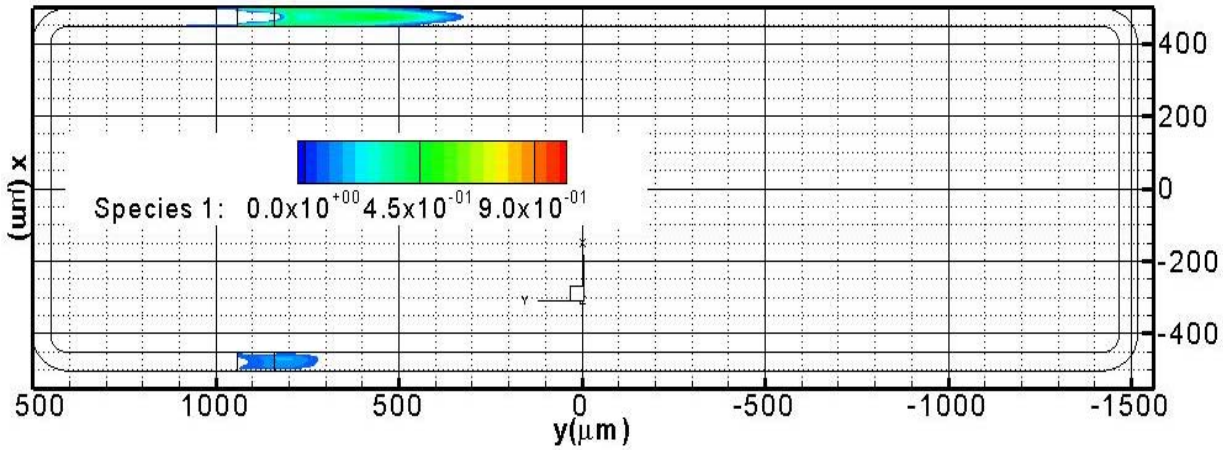

Figure3.16: Species plug at t=1.8sec shown on a section through the channel at Z=75 μm for case 2

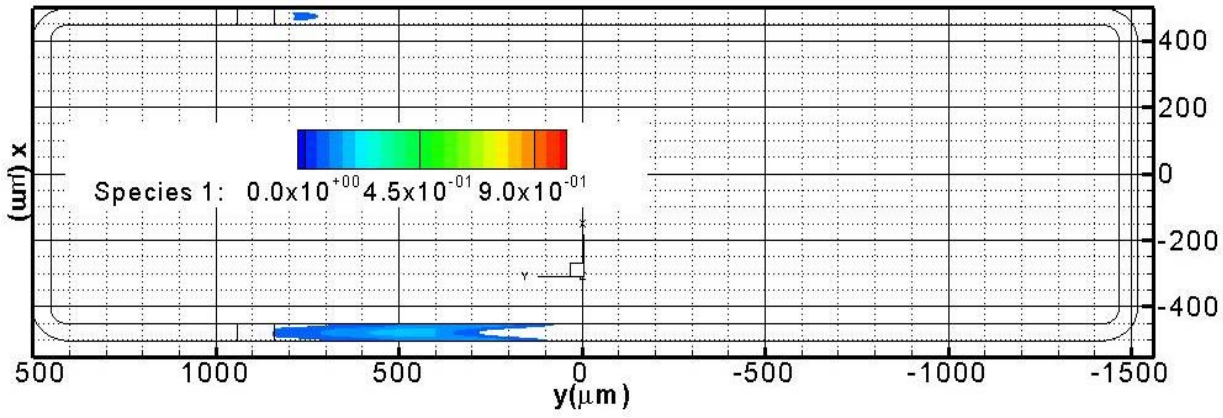

Figure3.17: Species plug at t=3sec shown on a section through the channel at Z=75 μm for case 2

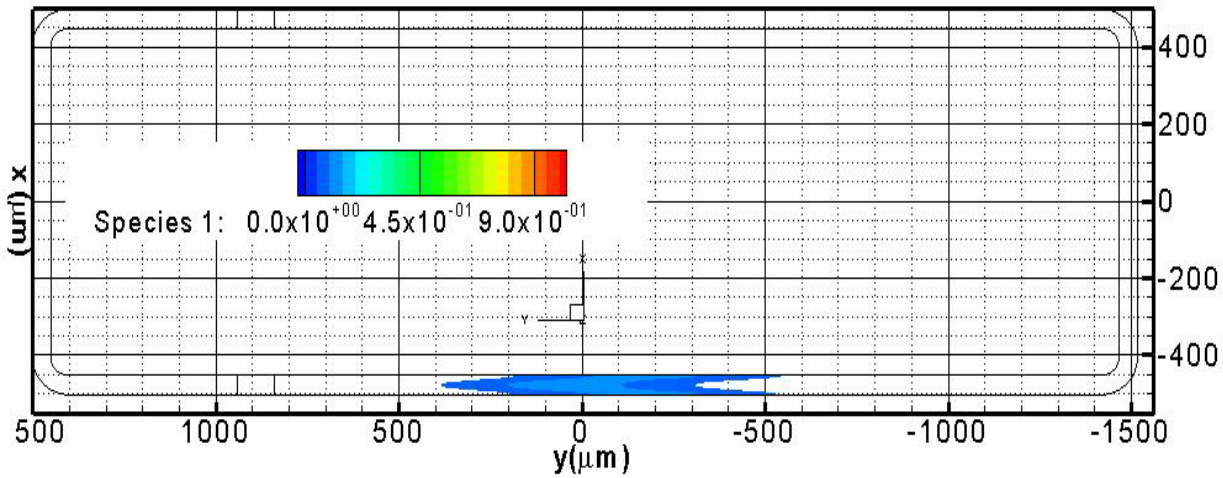

Figure3.18: Species plug at t=4.2sec shown on a section through the channel at Z=75 μm for case 2

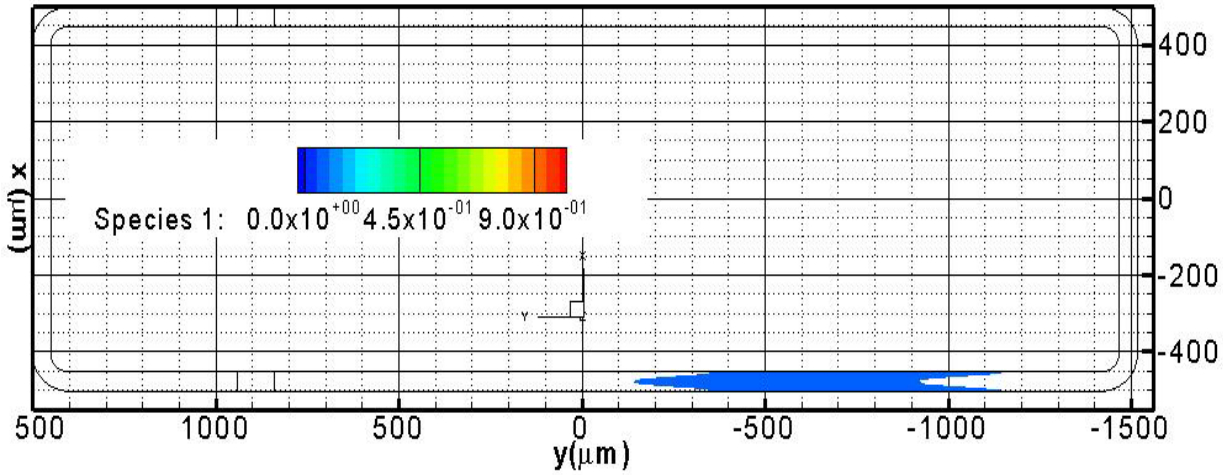

Figure3.19: Species plug at t=5.4sec shown on a section through the channel at Z=75 μm for case 2

3.4 Case3

The electroosmotic mobilities for this case were chosen so that again their ratio $\frac{\mu_{e1}}{\mu_{e_2}}$ is 1.5α. The difference between this case and the previous one is in the ratio of the electroosmiotic mobility to the electrophoretic mobility of the charged species. In this case this ratio is larger in absolute terms and equal to that of case 1. So the electroosmotic

flow that “carries” the charged species in the opposite direction to that dictated by electrophoresis is stronger.

3.4.1. Electroosmotic Mobilities

We kept the same boundary conditions as before, except for the electroosmotic mobilities. To achieve the new ratio we used

$$\mu_{e_1} = 71000 \mu m^2 / V.s$$
$$\mu_{e_2} = -17067 \mu m^2 / V.s$$

3.4.2 Results

As with the previous case and since we are again perturbing the optimum conditions, the pressure gradient is expected to be more important than in Case 1, which will induce a non-uniform flow profile. It is interesting to quantify how different the velocity gradient is, the magnitude of the velocity and the species motion.

3.4.2.1 Velocity profiles in the Straight Parts of the Channel Loop

The streamwise velocity distributions over the crossection of the straight portions of the channel are shown in Figures 3.20 and 3.21. In the straight parts of the loop, far from the corners and electrodes influence, for the Y=0 μm plane, we have the same maximum value of the velocity at the walls as in case1 because μ_{e_1} is the same. This is expected knowing that electroosmosis governs the flow near the walls. On the other hand the flow magnitude in the core of the channel is one third smaller than the one near the wall; this is due to the noticeably larger pressure gradient that developed as a result of the mobility/length ratio departure from the optimum value. This is also valid for X=0 μm plane, where the flow next to the wall is only due to electroosmosis and the core is influenced by the pressure gradient. It is important to notice that for both figures 3.20 and

3.21 we can see that the magnitude of the velocity in the core flow is the same. Let's now take a closer look to the values of velocities in both channels near the wall and interpret them.

This case satisfies the following relationship:

$$\left|\frac{\mu_{e1}}{\mu_{e2}}\right| = 1.5\alpha = 1.5\frac{L_1}{L_2},$$

i.e. the mobility ratio is 50% larger than the predicted optimum value, which leads to $\frac{|\mu_{e1}|}{L_1} = 1.5.\frac{|\mu_{e2}|}{L_2}$ and because $u_{ej} = \mu_{ej}.\frac{\Delta\Phi}{L}$ we have $|u_{e1}| = 1.5|u_{e2}|$, with u_{e1} and u_{e2} being the electroosmotic velocities immediately near the walls. So, we should expect a wall velocity in channel 1 that is, in absolute terms, roughly equal to 1.5 times velocity in channel 2, in regions far from the corners and the electrodes. In figures 3.24 and 3.25, we can see that u_{e1} is about 3000 $\mu m.s^{-1}$, while u_{e2} is about 2000 $\mu m.s^{-1}$, so that confirms our logical expectations of the velocities values next to the channel's inner walls.

Just like the two previous cases, the velocity profile in this case is symmetrical about the geometrical axes of symmetry and unidirectional.

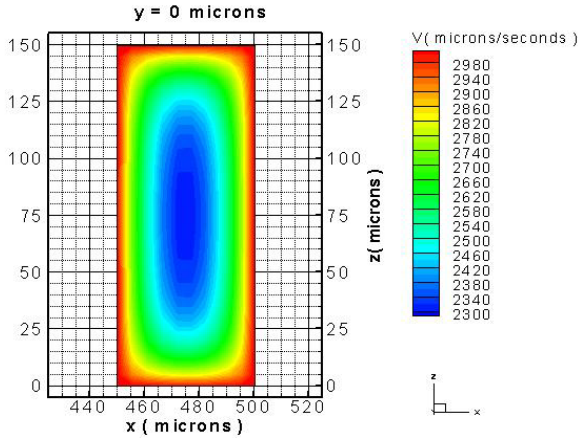

Fig 3.20: Stream wise velocity ($\mu m.s^{-1}$) distribution on the Y=0 μm plane for X>0 for case 3

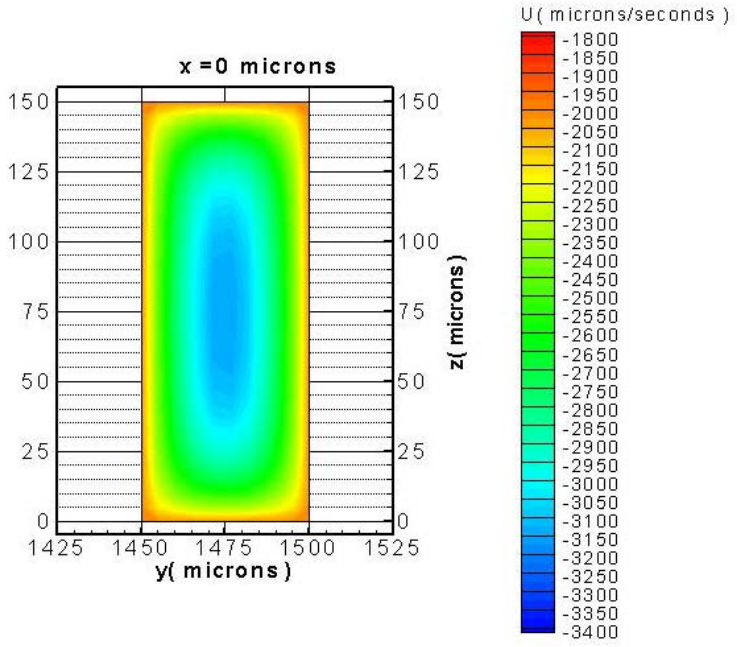

Fig 3.21: Stream wise velocity ($\mu m.s^{-1}$)distribution on the X=0 μm plane for Y>0 for case 3

3.4.2.2 Species Plug Evolution

Figures 3.22 to 3.27 show the progress of the species as it moves around the loop on the mid-plane of the channel loop. Successive representations are taken 1.2 sec apart. From the sequence of figures we observe that:

- Because the electroosmotic flow maximum magnitude is similar to the one in case1, and the species mobility is the same, the charged species moves around the loop at a comparable speed with case 1.
- Because of the development of a longitudinal pressure gradient (see discussion in a later section) and the distortion of the principal velocity component profile, the species is more distorted in the straight parts of the channel

- The species is also distorted as it goes around corners and more so after crossing the electrodes (these effects will be discussed in more detail separately in a later section).

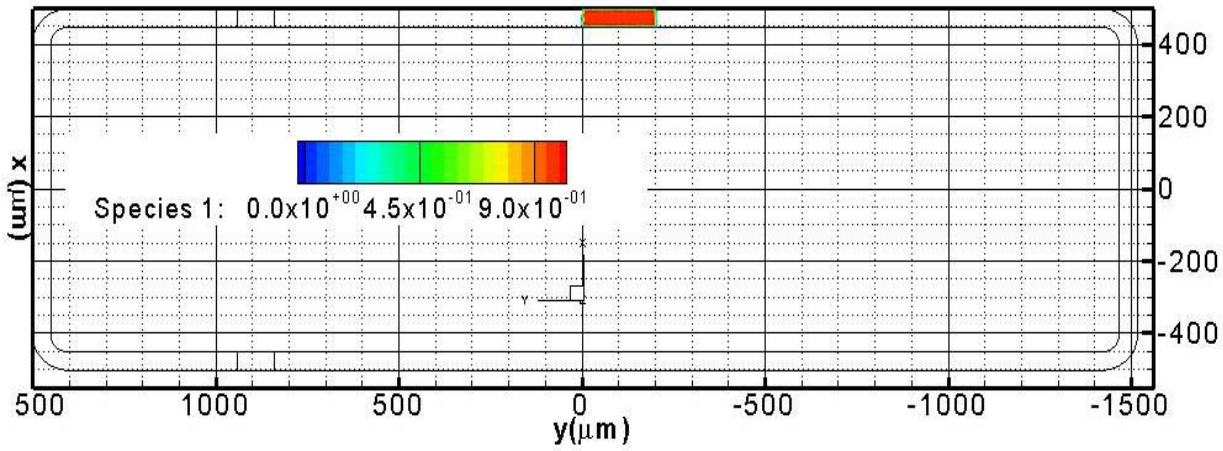

Figure3.22: Species plug at t=0sec shown on a section through the channel at Z=75 μm for case 3

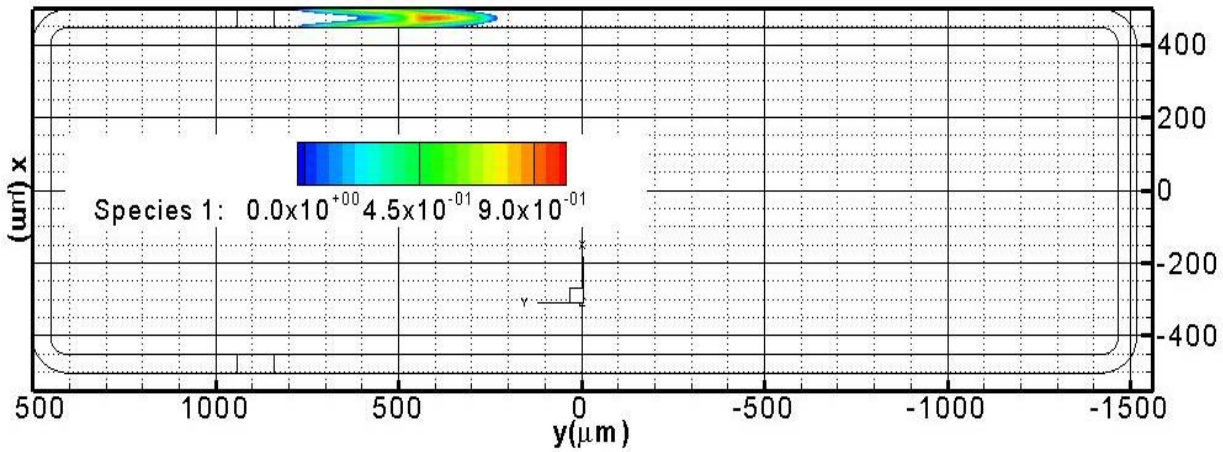

Figure3.23: Species plug at t=0.6sec shown on a section through the channel at Z=75 μm for case 3

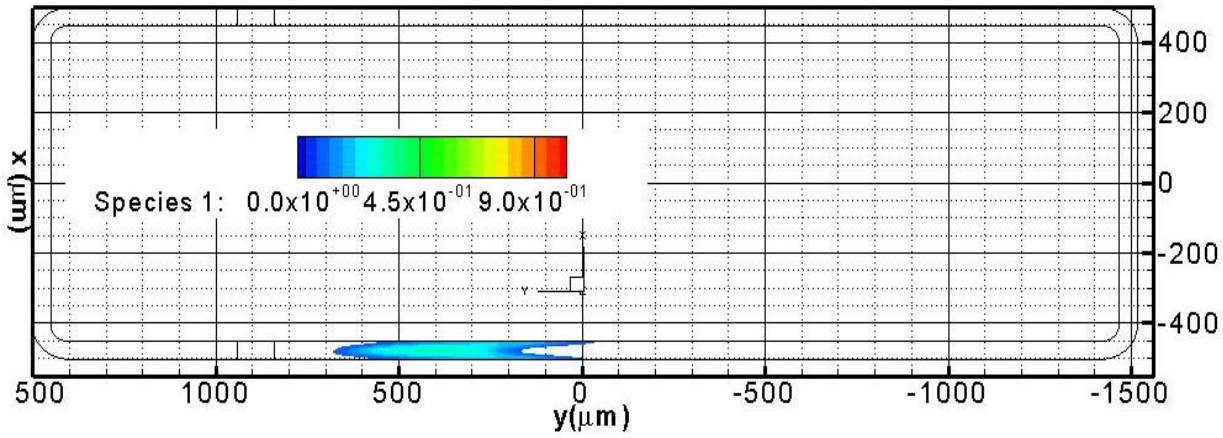

Figure3.24: Species plug at t=1.8sec shown on a section through the channel at Z=75 μm for case 3

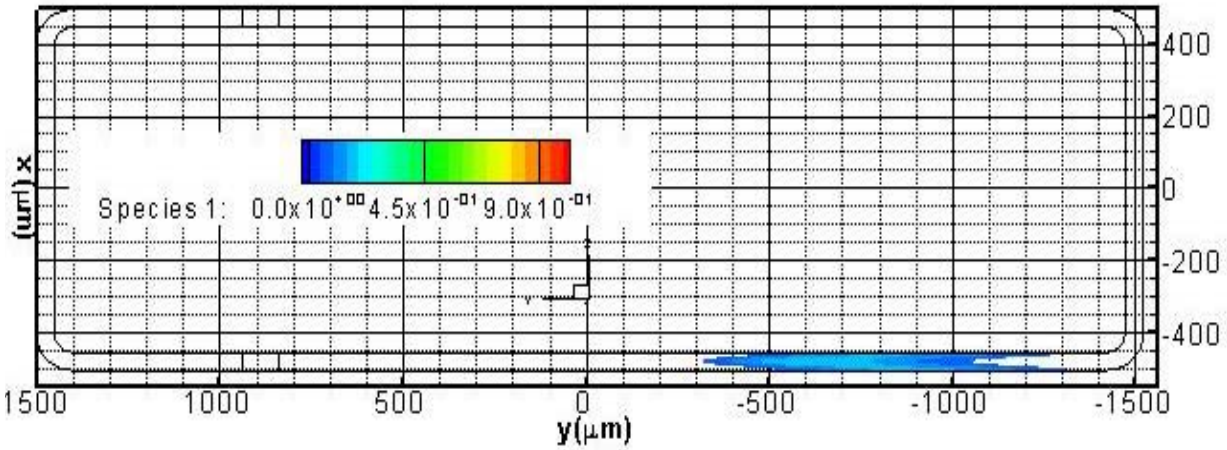

Figure3.25: Species plug at t=3.0sec shown on a section through the channel at Z=75 μm for case 3

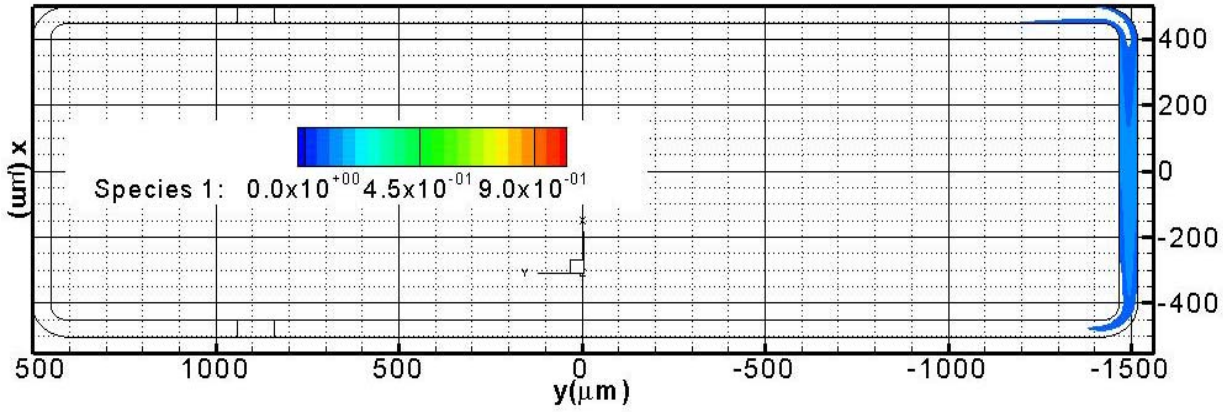

Figure3.26: Species plug at t=4.2sec shown on a section through the channel at Z=75 μm for case 3

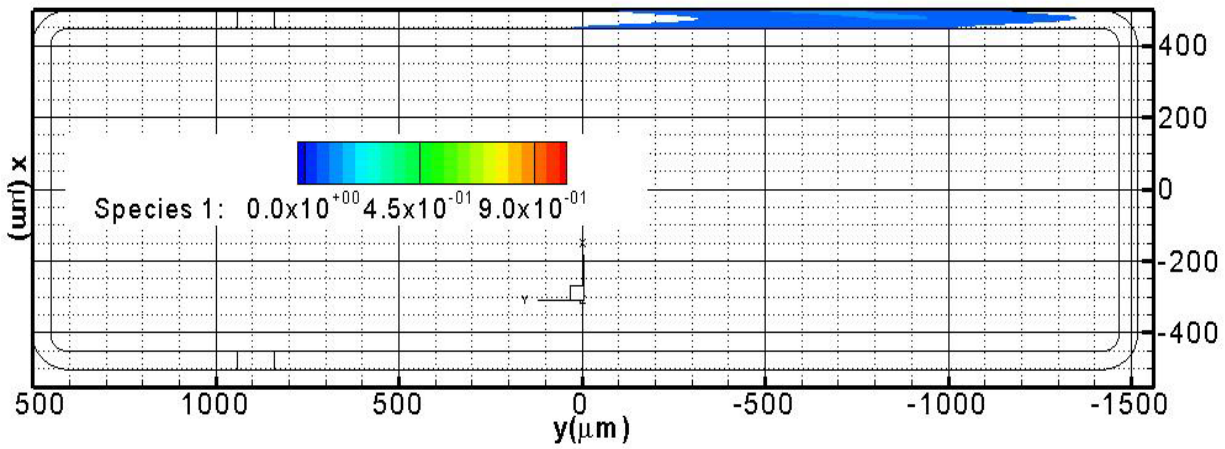

Figure3.27: Species plug at t=5.4sec shown on a section through the channel at Z=75 μm for case 3

3.5 Case 4

We chose the mobilities for this case such as their ratio $\frac{\mu_{e1}}{\mu_{e_2}}$ is 0.5α . This case is chosen to illustrate the functionality of the device when the mobility ratio is smaller than the optimum value α .

Also for the species to make a complete loop, it's important that μ_{e_1} is large enough compared to μ_{ep} . In this case this contrast is the same as in Cases 3 and 4.

3.5.1. Electroosmotic Mobilities

We kept the same boundary conditions as previously, except for the electroosmotic mobilities. To achieve the new ratio between them.

$$\mu_{e_1} = 71000 \mu m^2 / V.s$$
$$\mu_{e_e} = -51200 \mu m^2 / V.s$$

3.5.2 Results

As for all the previous cases, in this section, we will analyze the velocity distribution in the straight parts of the channels, and the species plug evolution.

3.5.2.1 Velocity Profiles in the Straight Parts of the Channel Loop

The streamwise velocity distribution over the crossection of the straight portions of the channel are shown in Figures 3.28 and 3.29. The velocity gradients in the cross-stream direction are three times more significant in this case that in the two previous cases. This is again because of the departure of the geometrical ratio from the theoretically optimum mobilities ratio, which leads to generation of a relatively higher pressure gradient throughout the loop. The flow magnitude is larger in this case more than any of the four previous cases, because of the larger electroosmotic mobilities. Indeed, the larger electroosmotic mobilities at the walls generate higher velocity magnitudes near the walls, and for the mobility proportions used for this case this leads to higher velocities in the core as well. Just like the three previous cases, the flow is unidirectional and symmetrical with respect to the both geometrical axes of symmetry. Looking at the velocities near the wall for figures 3.28 and 3.29 we can see that immediately near the walls the velocity in channel 1 is about 3200microns/seconds. On the other side of the loop, in channel 2 the velocity near the wall is about 6400microns/seconds with which, in absolute terms is again consistent with the expected $|u_{e1}| = 0.5|u_{e2}|$ from the set mobility ratio $\left|\frac{\mu_{e1}}{\mu_{e2}}\right| = 0.5.\frac{L_1}{L_2}$.

3.5.2.2 Species Plug Evolution

Figures 3.30 to 3.33 show the progress of the species as it moves around the loop on the mid-plane of the channel loop. Successive representations are taken $1.2\,\text{sec}$ apart. From the sequence of figures we observe that:

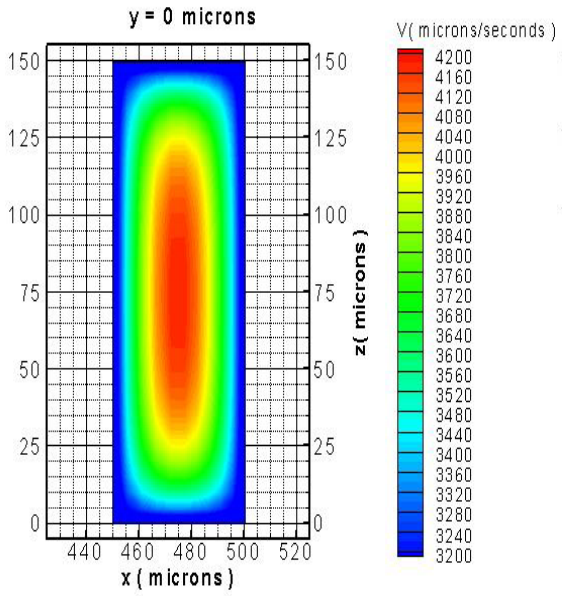

Fig 3.28: Stream wise velocity ($\mu m.s^{-1}$) distribution on the Y=0 μm plane for X>0 for case4

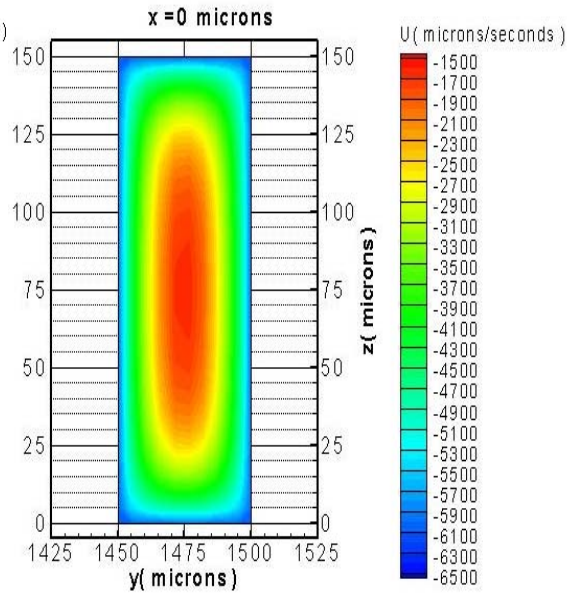

Fig 3.29: Stream wise velocity ($\mu m.s^{-1}$) distribution on the X=0 μm plane for Y>0 for case4

- distorted principal velocity profile discussed previously as a result of the fact that the mobility ratiodeparts by 50% from the theoretically optimum inducing a pressure gradient (discussed in a later section), which adds up to the geometrical factors to determine the shape of the plug
- A in the previous cases, under off-optimum conditions (Cases 2, 3) the species does move around the loop as expected from the predictions of the simple theory based on ducts of circular crossection.
- The species moves faster due to a stronger electroosmotic flow (larger absolute mobility values in channel 2 than previous cases)

The overall higher electroosmotic velocities help the movement of the species out of the electrode they prefer, in this case the anode. This point deserves the reader's attention. Because the charged species will tend to move towards and attach itself on

the electrode of preference under the electrophoretic effect, a strong electroosmotic flow, even with a strong hydrodynamic effect present, will tend to reduce the probability of the species to reach the electrode of preference.

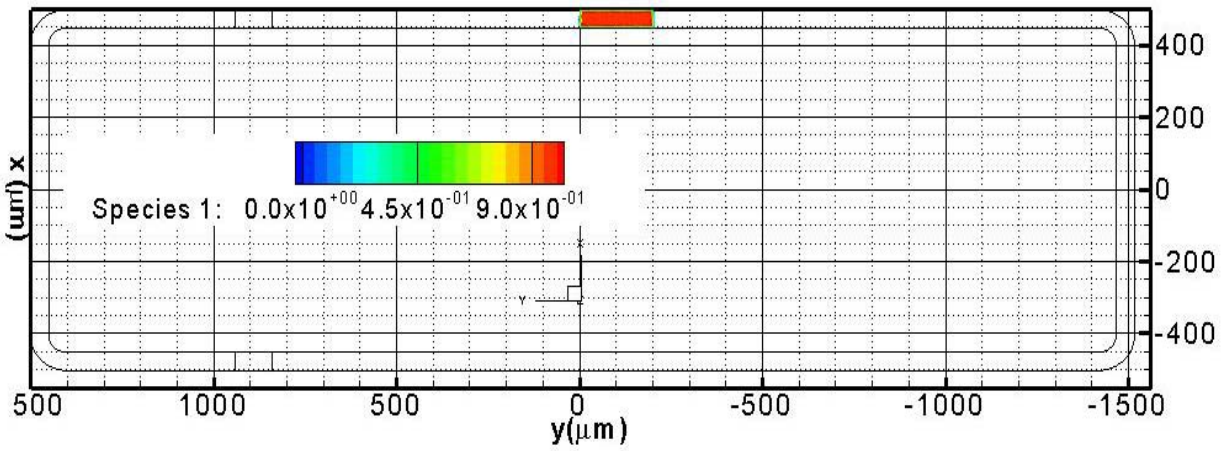

Figure3.30: Species plug at t=0sec shown on a section through the channel at Z=75 μm for case 4

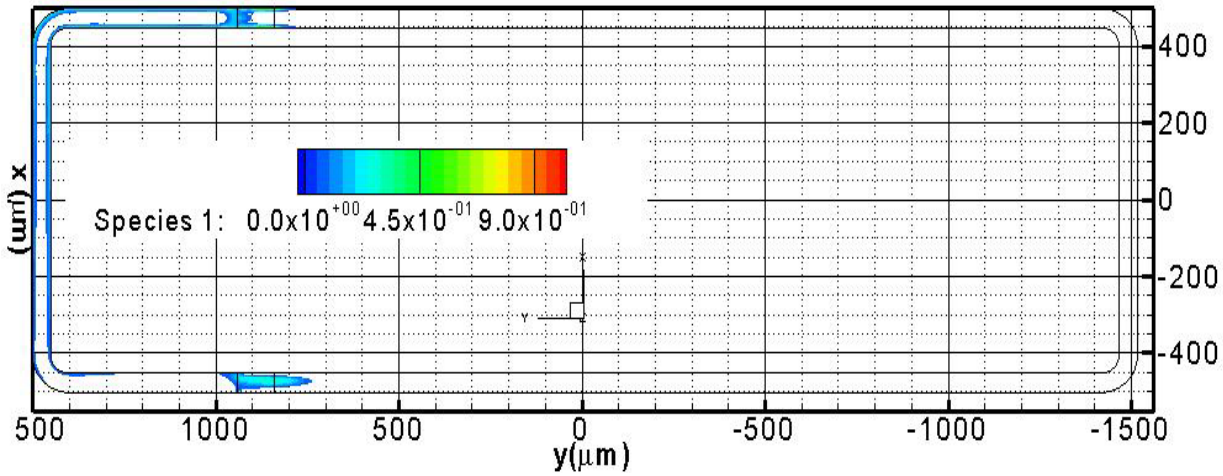

Figure3.31: Species plug at t=0.6sec shown on a section through the channel at Z=15 μm for case 4

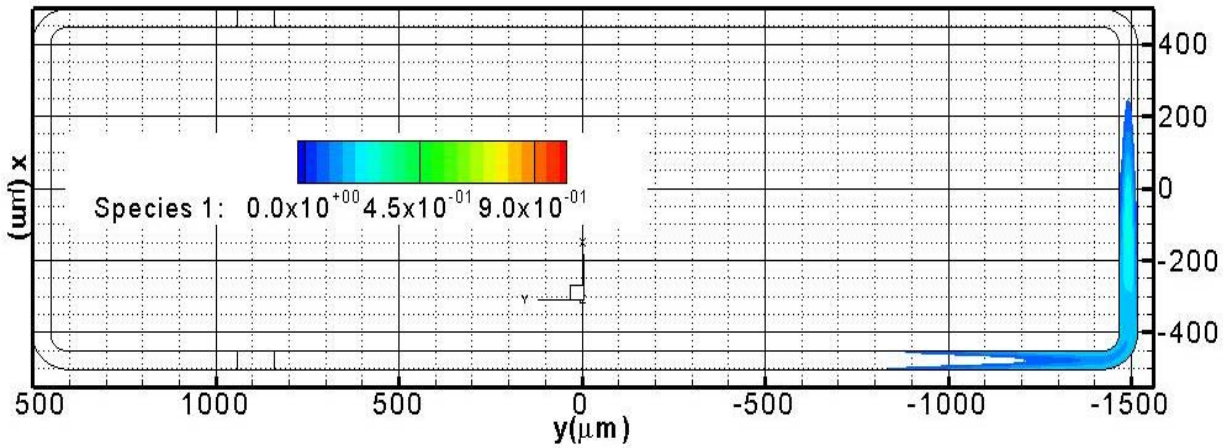

Figure3.32: Species plug at t=1.8sec shown on a section through the channel at Z=75 μm for case 4

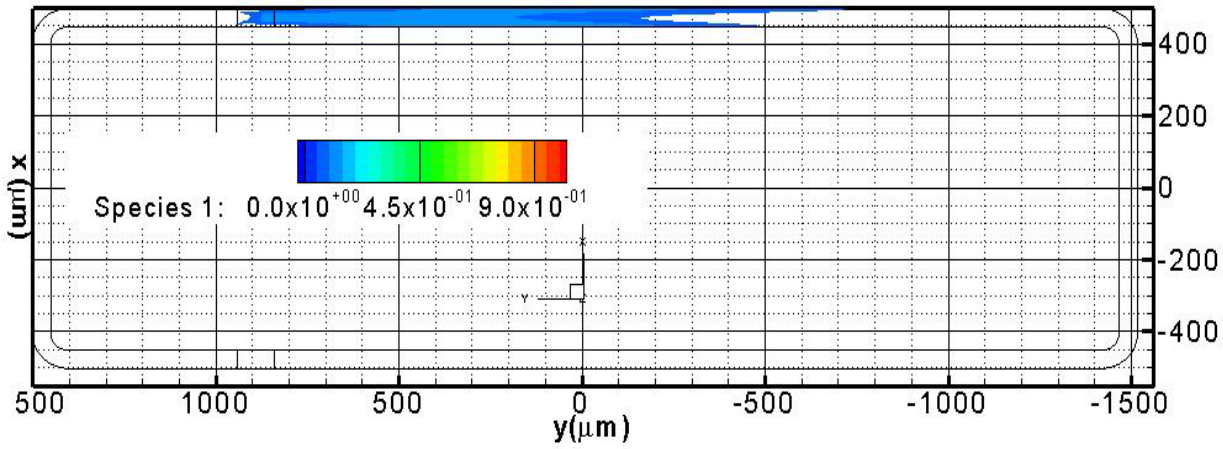

Figure3.33: Species plug at t=3.0sec shown on a section through the channel at Z=75 μm for case 4

3.6 Pressure Profiles

The pressure profiles (gauge) for the four cases presented previously are shown in Figures 3.34, 3.35, 3.36 and 3.37. It is evident the figures that the pressure gradient along the channel branches away from the electrodes in the first case is the smallest among all cases, which is what is expected according to the theoretical prediction knowing that in case 1 the mobility ratio and the length ratio are equal in terms of absolute values and opposite in terms of signs. This condition implies a pressure gradient that would tend to zero according to equation repeated here for convenience

$$\Delta p = \frac{8\mu}{a^2}\Delta\Phi.\frac{\frac{\mu_{e_1}}{L_1}+\frac{\mu_{e_2}}{L_2}}{\frac{1}{L_1}+\frac{1}{L_2}}$$

If we compare the pressure profiles from cases 2, 3 or 4 to the pressure profile form case 1, the contrast in terms of pressure magnitude along the channel is clearly significant, in all those cases this value is at least 5 to 10 times larger than in case1.

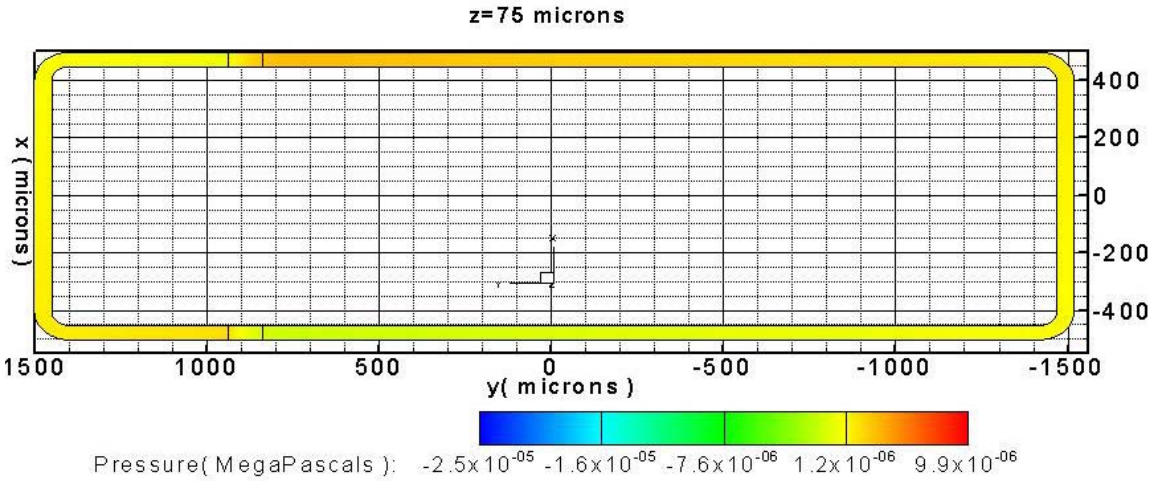

Fig 3.34: Gauge Pressure profile (MegaPascals) shown on a section through the channel at Z=75 μm for case 1

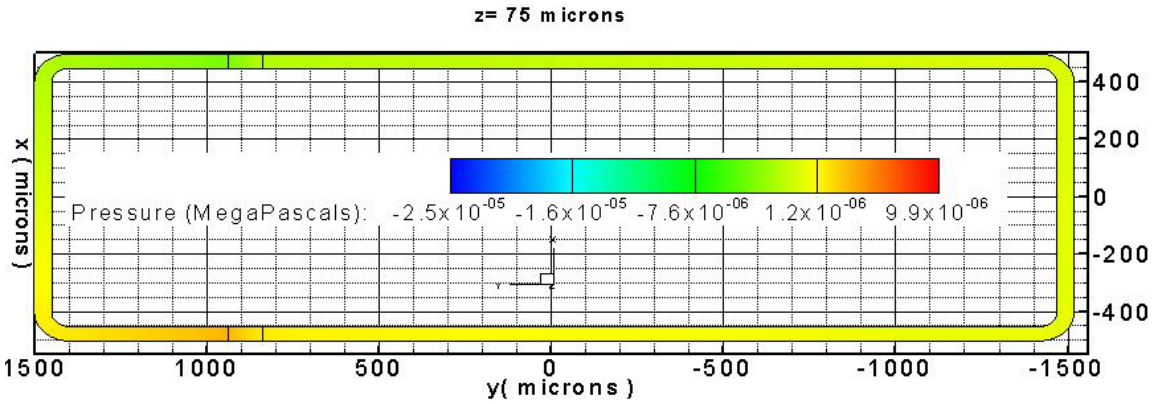

Fig 3.35: Gauge Pressure profile (MegaPascals) shown on a section through the channel at Z=75 μm for case 2

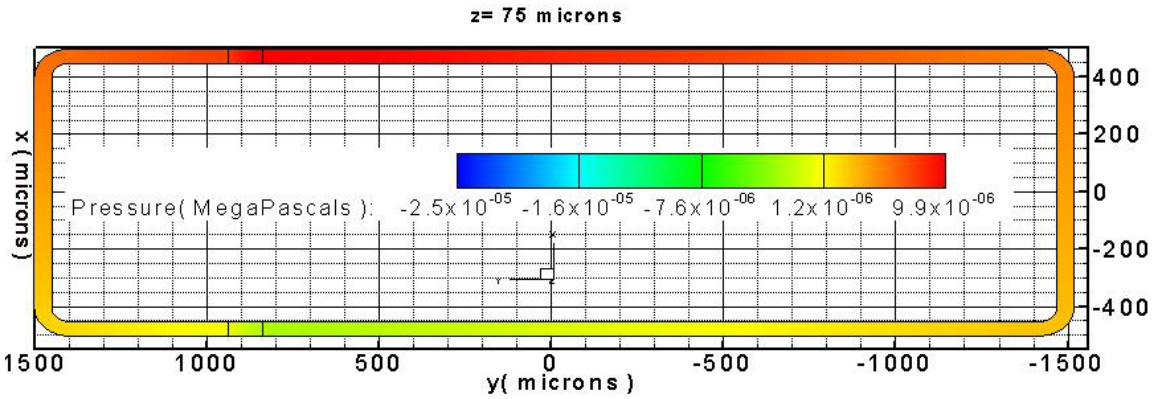

Fig 3.36: Gauge Pressure profile (MegaPascals) shown on a section through the channel at Z=75 μm for case 3

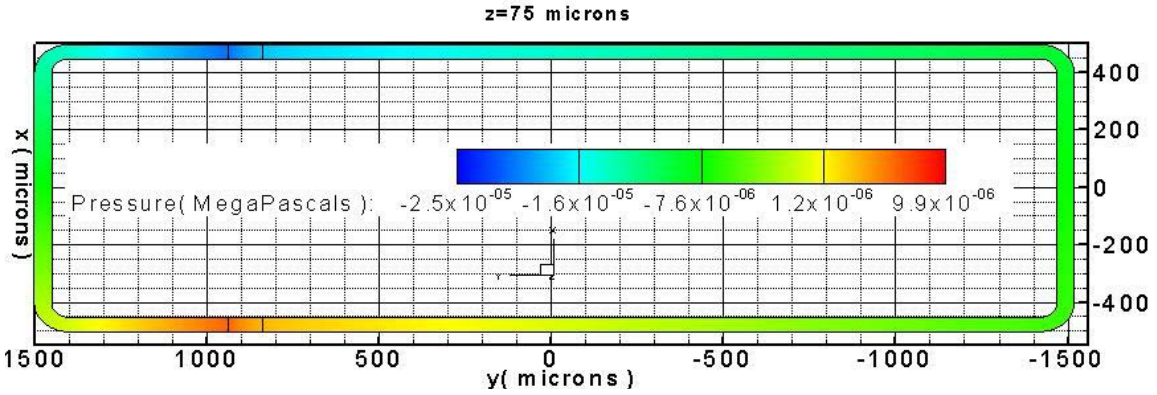

Fig 3.37: Pressure profile shown on a section through the channel at Z=75 μm for case 4

Let us now compare the pressure values between the cases that do develop a non-negligible pressure gradient. The pressure gradient expression that we have from the simple theory can be useful to compare cases 2, 3 or 4 to each other qualitatively.

From this equation we can state that the pressure gradient is proportional to $\Delta p \propto \frac{\mu_{e1} + \alpha.\mu_{e2}}{1+\alpha}$ with α being the length ratio. If we plug in the values for electroosmotic mobilities for each case and then compare the pressure gradient magnitudes and signs we can see that $\Delta p_2.\Delta p_3 > 0$ and that $\Delta p_2.\Delta p_4 < 0$ and $\Delta p_3.\Delta p_4 < 0$, that is verifiable using the proportionality expression listed above.

On the other hand, as far as magnitudes are concerned, we get that $\Delta p_3 \approx 1.3.\Delta p_2$ and that $\Delta p_4 \approx 3.\Delta p_3$ and this also can be verified from the pressure profiles shown in the relevant figures (3.34-3.37). In fact from Fig. 3.37 we estimate $\Delta p_4 \approx 2.10^{-5}$ MPa (MPa is MegaPascals) and from Fig. 3.36 we can estimate Δp_3 to be roughly equal to $\Delta p_3 \approx 7.10^{-6}$ MPa. The ratio $\Delta p_4 / \Delta p_3$ obtained from our simulations in rectangular channels including bends and electrodes, is consistent in magnitude with what we predicted from the analytical solution for a circular tube.

Similarly from Fig. 3.35 we can estimate the pressure difference between the two electrodes Δp_2 to be $\Delta p_2 \approx 5.5.10^{-6}\ MPa$ which again is consistent with the simple analytical result.

3.7 Flow Profiles in Non-Straight Parts of the Loop for Case1

So far, we have illustrated the flow properties in the straight parts of the channel, far from the electrodes region and from the corners and bends of the loop. The flow pattern was in agreement with what was expected from theory. In this section we will take a closer look to what happens to the flow and the species at the electrodes and the corners of the loop.

It is important for the following to highlight the geometrical fact that the electrode is entirely on the side of channel 1, therefore the whole region surrounding the electrode has the same electroosmotic mobility and the boundary between channel 1 and channel 2 is located at Y=940 μm . When we previously discussed the cyclic motion of the species we observed that the shape, concentration and progress of the species are highly influenced by the species path through the electrode region. Let us now look more closely

at the region under one of the electrodes. The behavior of the flow in the neighborhood of one electrode is the reverse of that in the other, so we will look at only one electrode instead of both of them.

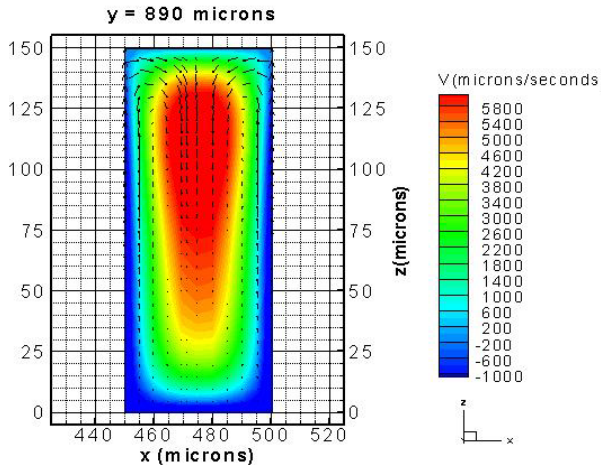

Figure 3.38: Streamwise velocity (V) distribution contours and secondary velocity vectors at the cathode longitudinal mid-plane (Y=890 μm)

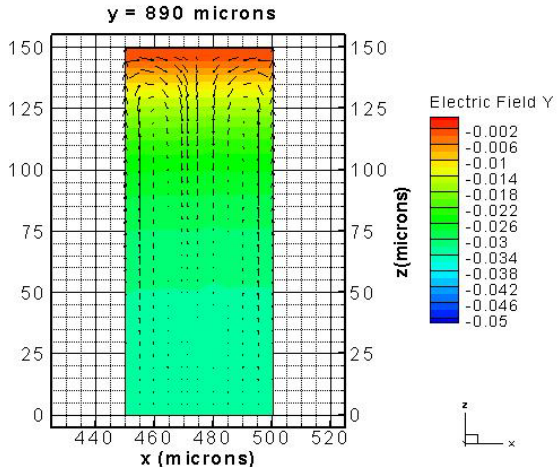

Figure 3.39: Streamwise electrical field distribution contours and secondary flow vectors at the cathode longitudinal mid-plane (Y=890 μm)

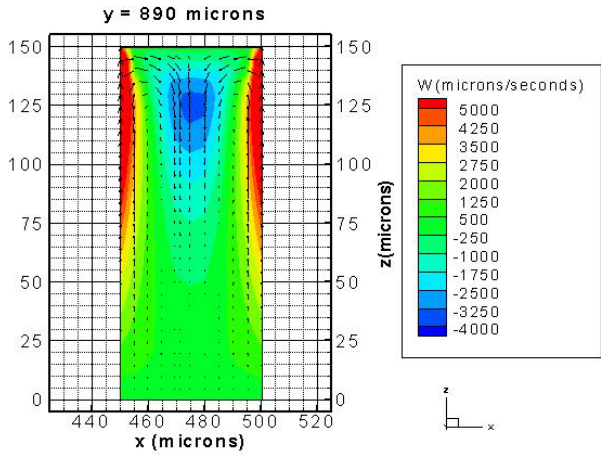

Figure 3.40: Cross-flow velocity (W) distribution contours and secondary flow vectors at the cathode longitudinal mid-plane Y=890 μm

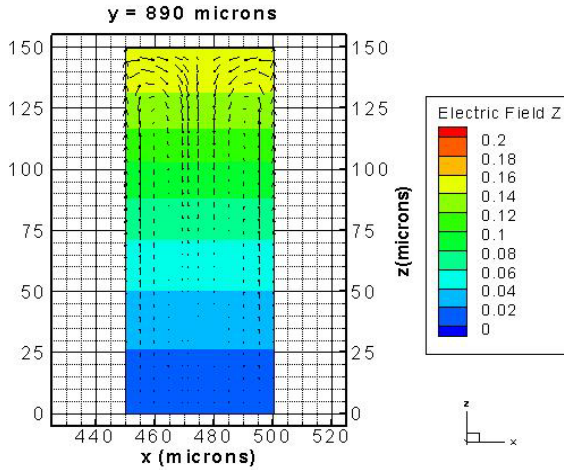

Figure 3.41: Distribution contours of the vertical component of the electrical field and secondary flow vectors at the cathode mid-plane Y=890 μm

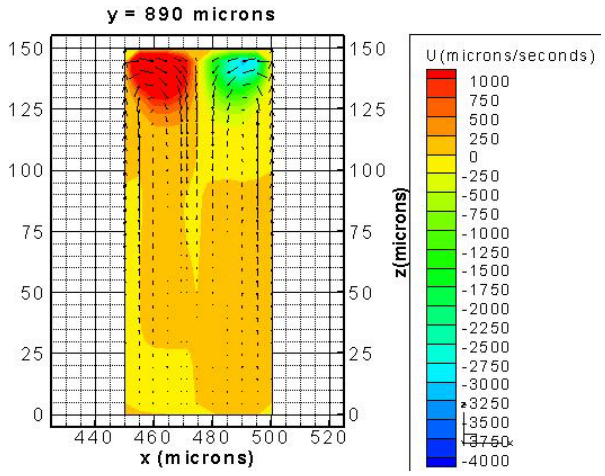

Figure 3.42: Cross-flow velocity (U) distribution contours and secondary flow vectors at the cathode longitudinal mid-plane Y=890 μm

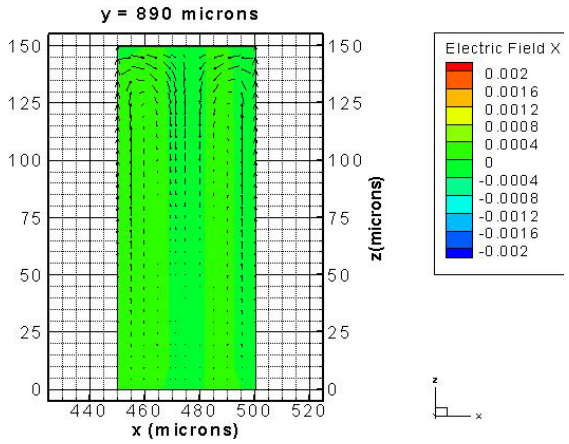

Figure 3.43: Cross-flow component distribution contours of the electrical field and secondary flow vectors at the cathode mid-plane Y=890 μm

As shown in Fig 3.0, which displays the geometry that has been used for all simulation cases, the cathode is situated at Z=150 μm, 840<Y<940 (μm), X>0; therefore the plane Y=890 μm is the middle plane of the electrode. Figures 3.38 to 3.43 show the flow features at that particular location. The flow in the neighborhood of the electrode is three-dimensional, in fact, we cannot overlook any component of the velocity in comparison to the other; all three of them have significant magnitudes. We notice that, while V and W magnitudes are comparable, and have substantial values all over the cross section, The cross-stream span wise velocity, U, is weak everywhere in the cross section, except for the immediate neighborhood of the electrode's surface. This feature can be explained by the proportionality between the electrical and velocity fields.

The presence of the electrodes at Z=150 microns induces a large electrical gradient in the Z direction as well as in the Y direction. Because the voltage is applied across the whole top width of the channel, there is no electrical field gradient in that particular location of the loop in the X-direction. One can also verify from figures 3.49, 3.51 and 3.53 that the Z- and Y-components of the electrical field are indeed larger than the X-component. On

the other hand, the velocity field and the electrical field are tightly related by $\vec{u}_{ej} = \mu_{ej}.\vec{E}$ on the boundaries, while in the interior of the flow under the electrodes hydrodynamic effects induce additional three-dimensional effects. One such hydrodynamic effect is manifested by the down-wards velocities which develop in the core of the channel under the electrode (see Figure 3.40) and the two opposite-sign span wise velocity regions immediately under the electrode (see Figure 3.42). The combined effect is illustrated in each of Figs 3.38-3.43 via the secondary velocity vector field. This secondary flow develops because fluid is brought upwards along the side walls because of the electrical field and is turned downwards to satisfy conservation of mass in the neighborhood of the electrode because it can not penetrate it. The opposite secondary flow that brings fluid downwards along the side-walls and upwards in the core of the crossection can be observed under the electrode of opposite sign (anode), which is not shown.

Now that we have an idea about what the flow is like at the middle section of the electrode, let us see how it is like elsewhere in the electrode region. It is interesting to investigate how the flow transitions from the straight part of channel 1 where there is no electrical field gradient, to the electrode region where there is a substantial electrical field gradient, and back to the straight part of channel 2 where the flow looks again fairly unidirectional before getting influenced by the corner of the loop.

Figure 3.44 represents the magnitude of the streamwise velocity flow at Y=750 microns which is located 90 microns below the downstream boundary of the cathode we can see that the flow is still fairly uniform and ranges around 3000 microns/second which is the value of the streamwise velocity of the flow in the straight parts of the channel in case1

as one can see in figures 3.4 and 3.5. As we approach the downstream boundary of the cathode located at Y=840microns , a velocity gradient starts developing in the Z-direction

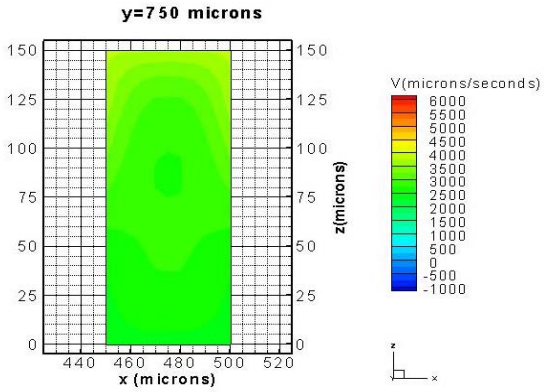

Fig 3.44: Streamwise Velocity (V) distribution contours before the electrode region (plane Y=750 μm)

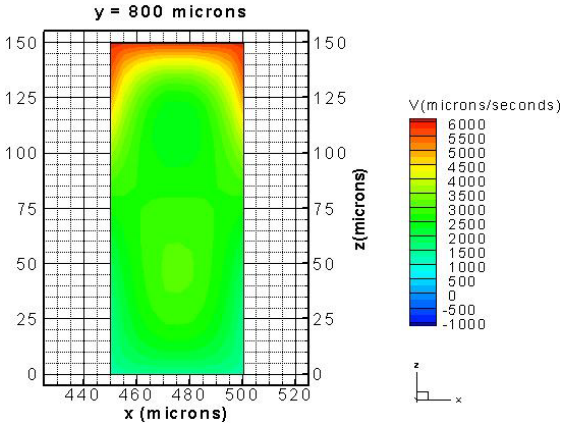

Fig 3.45: Streamwise Velocity (V) distribution contours immediately before the electrode region (plane Y=800 μm)

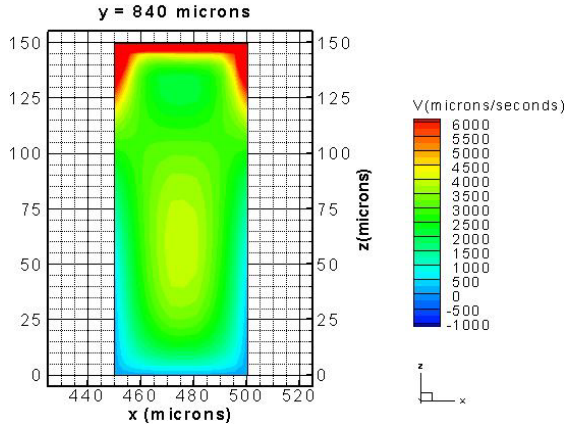

Fig3.46: Streamwise Velocity (V) distribution contours at the electrode's upstream boundary plane Y=840 μm.

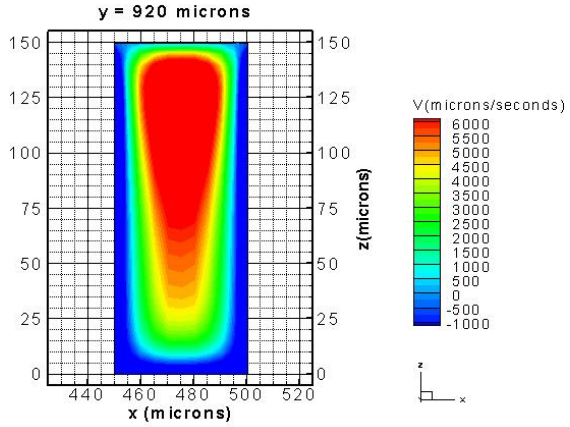

Fig3.47: Streamwise Velocity (V) distribution contours at the electrode's downstream boundary plane Y=920 μm.

(see Fig. 3.45, 3.46) and that is due to the electrical field gradient in both and Y ans Z directions in the electrode region, it might be useful to remind the reader of the proportionality between the velocity and electrical fields vectors to explain this velocity gradient at the entry of the electrodes region. The physical phenomena in the electrode region has been explained in the previous paragraph; and this is what gives the flow the pattern shown in Fig3.46 and 3.47: fluid is brought upward in the core region of the flow

to satisfy the duality between the electrical and velocity fields (as the electrical filed due to the presence of the electrodes develops), and fluid is brought downwards to satisfy the

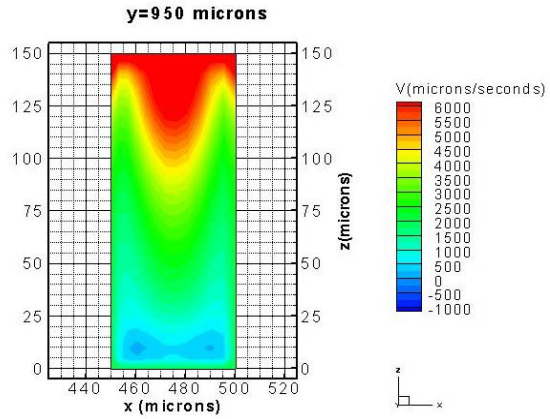

Fig3.48: Streamwise Velocity (V) distribution contours at the electrode's upstream boundary plane Y=950 μm.

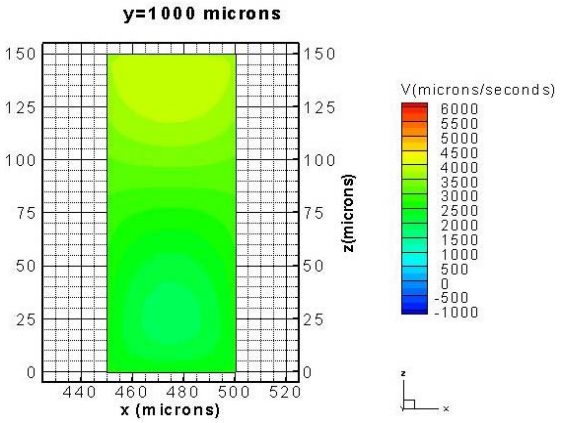

Fig3.49: Streamwise Velocity (V) distribution contours at the electrode's upstream boundary plane Y=1000 μm

conservation of mass knowing that it can not penetrate the electrode surface. Y=950 microns is located at the upstream boundary section of the cathode and the velocity magnitude there ranges from zero to 6000 microns/ second which is comparable to the streamwise velocity profile in Y-sections taken from 840 microns to 940 microns. Also,

this section is particularly interesting because not only is it the boundary of the electrode region but also the boundary between Channels 1 and 2, so one should predict a velocity profile that is fairly different from the pattern shown in the previous sections taken in the electrode region because of the change in the values of the electroosmotic mobility and thus in the boundary conditions for the velocities. On the other hand , we previously explained in the section dedicated to case1 that in the straight parts of the loop for that particular case , we should have the same velocity range for both channels as the ratio of lengths and electroosmotic mobilities are matching which makes the electroosmotic mobilities at the inner walls of the loop in the straight parts of it quiet equal. Therefore the streamwise velocity pattern in this section is not drastically different as we could have predicted, and that is due to the particularity of case1 that makes the flow magnitude profiles look the same everywhere in the straight parts of the whole loop. That being said, the streamwise velocity profile for Y=1000 microns (see Fig 3.49) makes sense in terms of range of magnitudes, being 60 microns above the upstream boundary of the cathode reduces sustainably the electrodes influences on the velocity profiles and makes it converge to the pattern that characterizes the flow in the straight parts of the loop in case 1 as shown in previous sections; from Fig3.49 we can see that the streamwise velocity magnitude is around 3000 microns/second which is close to what was shown in Fig3.4 and 3.5 and supports the observation that the flow looks the same before and after the electrode's boundary sections in case1 – and only case 1- because theoretically the velocity magnitudes are the same for channel's 1 and 2 immediately at the inner walls.

Chapter 4 EOF Measurements

As explained in the previous chapters, the core principle of the Modified Micro-Scale Electrophoretron is very dependant upon the electroosmotic mobilities of the two branches of the loop. It is then necessary to examine the feasibility of appropriate values for these properties i.e. the values of μ_1 and μ_2. That is a critical step before designing a chip because the architecture of the loop is closely related to the ratio μ_1 / μ_2.

To make the EOF measurements, before and after surface modification, we used the "current-monitoring method" established by Zare et al.(1988). The method is based upon the difference of resistance of a channel that would be exposed to two different concentrations of the same buffer. Let's assume that we have a straight micro-channel with its two ends connected to reservoirs to accommodate electrodes. After we fill the channel and both reservoirs (hydrodynamically by pushing the fluid with a syringe pump) with a buffer of concentration c_1 we apply a voltage difference and we wait for the current to stabilize around a certain value. This value reflects the resistance of the channel for this concentration.

Then, using a syringe pump, we empty the reservoir from which the buffer is moving away- that would be the anode- if we are in presence of positive EOF, and we put a solution of concentration c_2 so that $c_2 > c_1$, usually $c_1 = 0.8c_2$. This last operation is quiet delicate and needs further description; in order to empty the reservoir safely we need to, first , switch off the voltage, remove the electrode that was immersed in the reservoir of interest , pump out the fluid from the reservoir using a syringe pump , fill the reservoir with the second buffer, put the electrode back in the reservoir and switch the voltage back on. One needs to be aware that these successive manipulations could highly

disturb the flow in the microchannel and could even explain the disparities in terms of EOF magnitude from one experiment to another. Other methods of EOF measurements that have a higher level of accuracy do exist but were not available yet while making those experiments. It might be useful to precise that the purpose of those initial measurements was to have an idea about the flow magnitude and directions in different materials before and after surface modification and investigate the EOF reversal feasibility, and with these objectives the current monitoring method with all its intricacies seemed to be a good start. After introducing this higher concentration buffer, the response-current of the chip is supposed to increase because the ionic strength of the second solution is higher. The current keeps increasing as long as there is a concentration gradient in the channel. As soon as the second solution reaches the cathode and the concentration is equal to c_2 everywhere, the current stabilizes again at a higher value. The time that this process takes depends on the speed of the electroosmotic flow in the channel (if the operation of changing concentrations is done with delicacy, the influence of hydrodynamic flow can be considered negligible). Because the velocity is directly proportional to the mobility

$$u = \mu_{eo}.\frac{\Delta\Phi}{L}, \qquad \textbf{(4.1)}$$

this latter can be deduced if we know the length of the microchannel and the electric field that has been applied during the experiment.

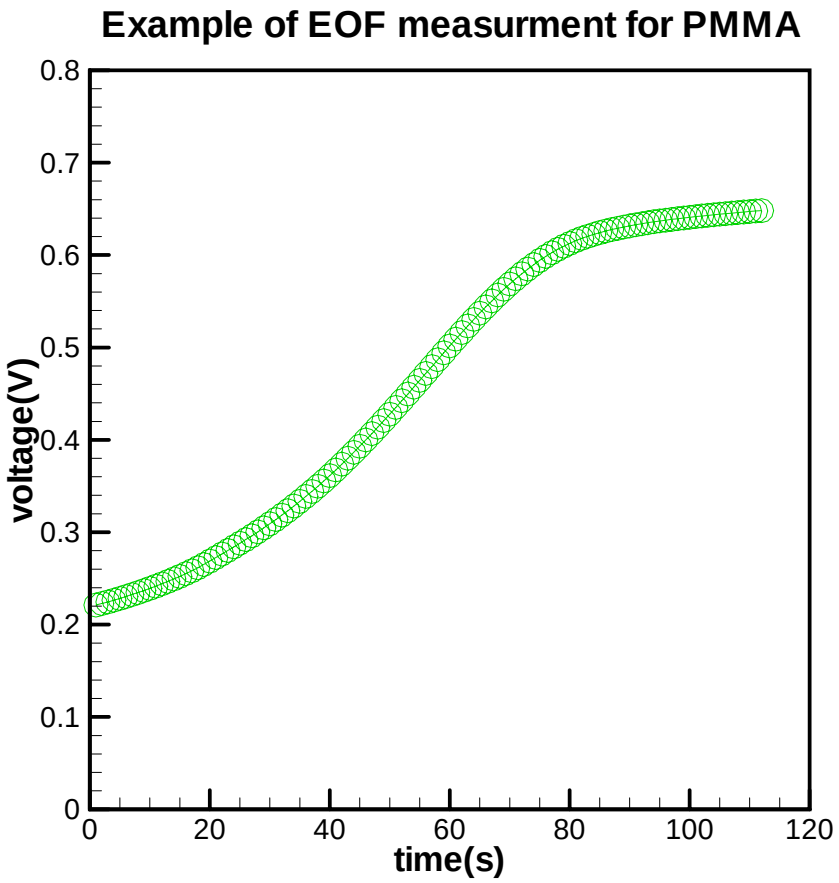

Figure4.1: A typical voltage vs. time signal segment indicating the transient process leading from the low ionic concentration plateau (left) to the high ionic concentration plateau (left) from an EOF measuring experiment in a Polymethylmethacrylate (PMMA) channel.

Figure 4.1 shows an example of the voltage signal from an EOF measurement on a PMMA channel while using the current monitoring method. Figure4.2 shows a corresponding example for the same measurement on a PC channel. One can notice that the outcome signal here is a voltage instead of a current, the reason behind this representation is that the experimental set up is such as we are measuring the voltage variation on a resistance where the current that we are trying to measure goes through. The current that we are interested in and the voltage that we get as an outcome are directly proportional.

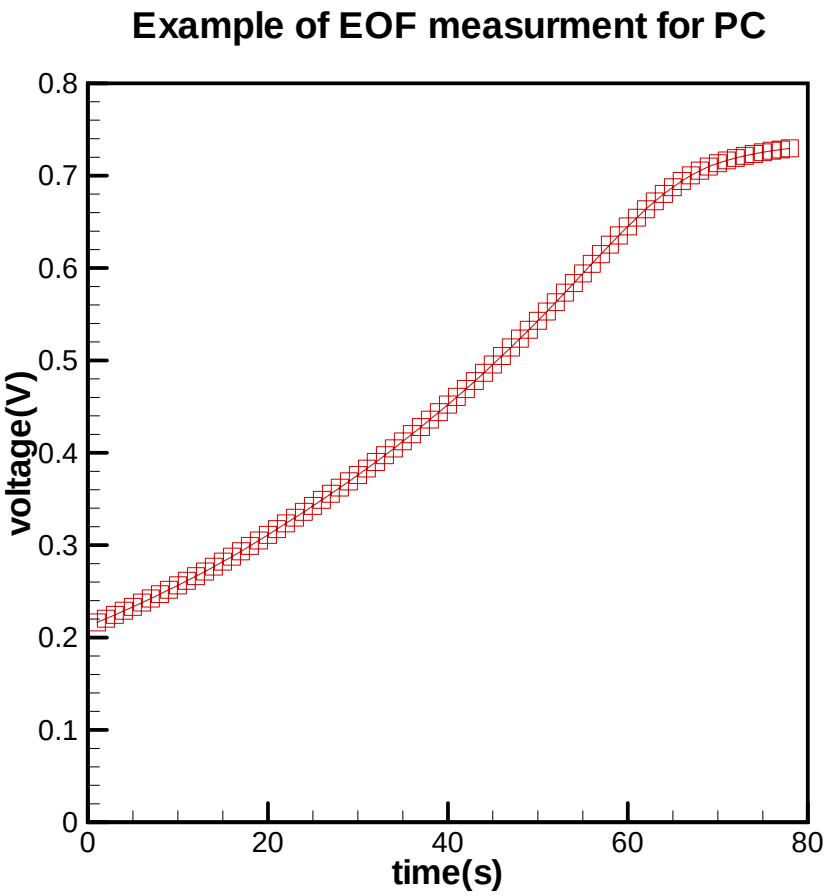

Figure4.2: A typical voltage vs. time signal segment indicating the transient process leading from the low ionic concentration plateau (left) to the high ionic concentration plateau (left) from an EOF measuring experiment in a Polycarbonate (PC) channel.

The time that the current (represented here by a voltage) takes to go from its lower plateau value to its higher plateau value as it stabilizes is the time that it takes for the channel and reservoirs to attain the same concentration. In fact, when the concentration reaches a value c_1 in this system, then the current (here voltage) becomes stable at a certain constant low value because the resistance of the channel (which is tightly related to the concentration of the buffer that fills it) is constant. After we fill the first reservoir with c_2 solution, ions start moving to the opposite sign electrode causing the concentration, thus the resistance, of the channel to vary and subsequently causing the

current (expressed in terms of a proportional voltage) to vary. As soon as the concentration reaches the same value again everywhere in the system the signal stabilizes at a new, higher value. The time that it took for the voltage (current) to move from the first stable value to the second stable value is representative of the electroosmotic flow of the channel.

Using equation (4.1) and estimating the velocity as $u = \frac{L}{\Delta t}$, we can retrieve the value of the mobility if we know the channel's length and the voltage difference applied at the electrodes.

EOF measurements have been conducted in Polymethylmethacrylate (PMMA) because it is convenient for surface modification purposes through the process we have chosen as appropriate for the application (described later). It is important to bear in mind that PMMA is not the best material that one can choose taking into consideration the thermal-cycling applications for which the modified micro-scale electrophoretron is being designed for (PCR, LDR etc). Its glass transition temperature (~104^{o}C) is pretty close to the highest temperatures (~95^{o}C) that are used in such applications. This does not entirely rule out the use of PMMA for such applications, especially if the thermal control is good enough to avoid overshoots that would create local hot spots approaching or exceeding the glass transition temperature. Nevertheless, the feasibility of surface modification in other materials with much safer higher glass transition temperature (~150-155^{o}C) such as Polycarbonate (PC) has also been investigated.

4.1 EOF Measurement in Pristine PMMA

In what follows we give an explicit description of the steps taken to achieve EOF measurements in pristine PMMA micro-fluidic chips. For all our measurements we used

channels with the same dimensions. Our channels were all $3cm$ long, $100\mu m$ wide and $70\mu m$ deep.

The channels that have been used for such EOF measurements were all obtained through hot embossing into PMMA sheets using a pre-fabricated mold insert. The mold insert is heated to $180^0 c$ and pressed into PMMA sheets with a force of $1000lb$ for $4.5mn$. After hot-embossing the micro-channels they were thermally bonded to PMMA cover-plates. The thermal bonding process is to be thoroughly exposed in the next paragraph. As the surface properties of both the micro-channels and the cover plate are critical to the experiment that they are going to be used for, it is important to make sure that they both are from the same source (and preferably the same batch) this makes them more likely to have the same surface properties to begin with.

It is also important to make sure that the thickness of the cover plate is less than the working distance of the microscope that is used to observe the channel after annealing.

4.1.1 Preparation Procedure of the PMMA Micro-fluidic Chips

Right after hot embossing, cutting excess material off and mechanically drilling $1mm$-diameter holes at the ends of the channel to make the reservoirs, the chips are not yet ready for use. The following steps that should be carried out in order to prepare the chips for EOF measurements:

1-Thoroughly clean the chips with detergent soap and distilled water to remove oil and dirt.

2-Sonicate them for a few seconds on both sides to remove any particle that could be stuck in the micro-device

3-Rinse with propanol (any alcohol is fine to use)

4-Rinse them again with distilled water.

5-Dry them using a pure (uncontaminated) air jet.

6-Inspect them under a microscope to detect any micro fabrication imperfections or particles that are still there even after sonication.

If any of the steps above are missed. The whole process should be repeated.

If after examination with the microscope, we see that the cross-section of the channel is not uniform, then it can't be used because imperfections due to the fabrication process can potentially bias the EOF measurements (e.g. by creating a relatively important hydrodynamic flow).

4.1.2 Thermal Bonding of the Cover

Cover plates are cut in a band saw in the same size of the micro-channel substrate. Cover plates come with a safety film that we remove right before thermal bonding so we don't need further preparation for them. The next step is to sandwich the microdevice-cover plate between two $0.5cm$ thick glass plates and to use paper clips (or a specialized jig if available) to keep everything altogether. We put that in the oven for 20 min at 107 degrees. It's been proven empirically that this was the right temperature to anneal pristine PMMA.

It is always better to let the assembly stand for a few minutes after the thermal bonding before removing the clips. After that we have to check if the chips have been properly annealed

-If we can peel off the cover plate with bare hands, that means that they are not annealed properly

-If after running distilled water in the channel using an appropriate syringe pump, we observe leakage, it means that the channel cannot be used.

-If we can see through a microscope, that there is a bubble somewhere in the chip; It is a sign that the chip has not been annealed properly because air has been trapped at some point of the process and the chip may not be useable.

-If, using a microscope, we can see particle(s) is blocking the channel; there is no point of using it for EOF measurements

-If, either because the temperature during thermal bonding was a little too high or the time the chips were in the oven was too long, the channel's walls are collapsed (especially in the reservoirs zone, making it impossible to run fluid into or out of the channel), then, evidently the chip is of no use.

If none of the above has been noticed, then the chip is good to use.

4.1.3 Buffers

EOF results are tightly related to the buffer that is used for the measurements. For the simple reason that the electroosmotic mobility of a material is very dependant upon

-the pH of the buffer

-the ionic strength of the buffer

So, for reliable results, we had to make sure that the buffer that is going to be used for those measurements has as close characteristics as possible to the one that is going to be used for the actual device.

PCR reactions are part of DNA assays. Most likely, upon using the device for the PCR reaction, the DNA is going to be introduced to the channel in a cocktail that is made with Tris-HCl buffer that has a pH of 8.3.

That is why we first made two different concentration solutions of Tris-HCL (18mM and 20mM), both having a pH of 8.3 for the EOF measurements. We had a hard time having a stable signal using this buffer, so we switched to a more popular one as far as EOF measurements are concerned, namely TBE. TBE stands for Tris-Boric-Ethylenediaminetetraacetic, it's a mixture of Tris base, Boric acid, EDTA (Ethylenediaminetetraacetic) and water. So we used two solutions of TBE with two different concentrations (1X and 5X), we made sure to adjust the PH of these two solutions to 8.3. The X notation in the concentration expressions is widely used chemistry labs and simply means that the 5X solution is 5 times more concentrated than the 1X solution. In this case 1X is 1M.

4.1.4 Voltage

We applied a potential difference of 405V over a 3cm long channel. That gives en electric field in the range of [100V/cm, 300V/cm] which is acceptable.

4.1.5 Results

Because the experimental process for EOF measurements leaves room for a lot of potential uncertainties and the electroosmotic mobility value is a very critical parameter for the design of the chip, the same experiment was repeated several times (20 times). Each experiment yielded one measurement of the EOF and an average value and a standard deviation value were computed over all the results so that a statistical confidence interval can be provided.

The advantage from doing such a big number of experiments is to also evaluate the repeatability of the process. From the interval of values of mobility that we got we can draw certain conclusions

Table4.1: EOF measurements for PMMA

Experiment number	Observed Δt (s)	Calculated μ_e ($cm^2/V.s$)
1	102	2.18
2	116	1.9
3	108	2.04
4	104	2.12
5	200	1.05
6	263	0.81
7	112	1.97
8	75	2.96
9	367	0.58
10	126	1.75
11	101	2.18
12	109	2.02
13	101	2.18
14	136	1.62
15	141	1.56
16	75	2.92
17	72	3.07
18	70	3.15
19	84	2.62
20	125	1.76

-the difference from the minimum and maximum value is quite important but this is expected considering the nature of the current monitoring method.

-One should take into consideration a range of values versus a value when it comes to mobilities, especially for design purposes.

Based on the experimental results, the average mobility of pristine PMMA in TBE buffer with pH=8.3 is $\boldsymbol{2.022 \pm 0.33 cm^2 / V.s}$ at 95% confidence level.

This value is very comparable to values already listed in the literature that were obtained using the same method.

4.2. Process to Produce NH_2-Modified PMMA

As we mentioned in Chapter 2, one fundamental condition for the device to work is to achieve opposite sign mobilities in the two branches of the loop. We said previously that PMMA has been chosen because of its convenience as far as surface modification goes. Soper et al. (2000) proved that amination of PMMA–attachment of amine groups to the polymer's surface-reverses the direction of its electroosmotic flow. One way to do so is to attach carboxylic groups to this surface via UV-Activation and then to bond those carboxylic groups to the Amine-terminations using 1-ethyl-3-(3-dimethylaminopropyl) carbodiimide hydrochloride (EDC) as a catalyst. There are other ways to attach Amine groups to the surface without using the UV-activation method, but we consciously chose this technique because of design considerations. One proven way of reversing the EOF in PC (which is the material of choice for our device) is to apply polybrene (PB) treatment to the surface of the channel, this is impossible to use in our case because we would have to chemically treat the surface of the channel after annealing the cover plate to the microdevice because thermal bonding a PB-treated microchannel to a PB-treated cover

plate is practically impossible. If we attempt to introduce the polybrene into the loop after thermal bonding the microchannel to the cover plate, we would induce a chemical treatment for all the inner surfaces in the loop and thus a reversed EOF everywhere in the microchannel while the purpose of using chemical treatment is the create opposite sign EOF in the two different branches of the microdevice.

We conclude that the treatment to be used for EOF reversal has to be applied to the branch of choice before the thermal bonding process. Knowing the effect of UV on the polymer surface and the chemical reaction that's prone to happen between the carboxylic termination and the amine group, we thought about investigating the effectiveness of this surface modification technique on both PC and PMMA.

4.2.1 UV-Activation

After cleaning the chips just like described in a previous section, and before annealing, UV-Activation is performed.

Soper and Murphy (2004) demonstrated experimentally that the longer the time exposure of the chips, the more carboxylic groups are formed on the surface, the more amine terminations are going to be attached, and the stronger the reversed EOF is going to be.

However, by choosing the option of a long UV exposure we take the risk of damaging the polymer's surface. Therefore, considering these two facts, we chose to maximize our chances of EOF reversal by choosing a relatively high exposure duration, yet small enough to avoid any surface damage or at least to keep it at a minimum.

Both the micro-devices and the cover slips were exposed to UV-Light for $20\ min$ at $1\,cm$ distance from a $254\ nm$ light source with a power density of $15\,mw.cm^{-2}$. It is

important to expose the two parts of the chip to the same amount of UV-radiation for the same duration. That way we expect both surfaces to be modified to the same extent, otherwise we might encounter difficulties while trying to thermally bond them, or more importantly they may develop different mobilities.

The next step is to clean the microdevice and the cover plate with distilled water, and dry them both very well and very quickly because the UV exposure turns the polymer's surface to become hydrophilic so water tends to adhere and makes the annealing quite hard to happen. The trick then is to dry the parts right after rinsing with water, and then to put them in the oven as soon as possible.

4.2.2 Thermal Bonding

This step is exactly the same as described earlier, the only difference lies into the temperature that we need to chose. It has been determined empirically to be around 102 degrees. We also need to run the same checking tests after the chips are out of the oven to see if they are usable or not.

4.2.3 Amination

One widely used solution for amination purposes is an Ethylendiamine solution. This solution is commercialized in a very concentrated form (99%). Furthermore, it is an organic solution so if we run it in channels in its pure state and let them stand for a little while for the reaction to occur, they are going to be clogged because after the liquid evaporates, the organic particles deposit into the channel and block it. So we need to dilute it, preferably in a phosphate buffer. The solution that has been used has a $5\,mM$ concentration. In $1\,ml$ of phosphate buffer of pH=7, we add $15\,\mu l$ of Ethylendiamine solution and 1mg of EDC (it is quantified in grams because EDC is a powder). The

different added substances have been quantified to have a final solution of $5\,mM$. We run this solution into the UV-Activated channels using a syringe pump and let them stand for a couple of hours at least and overnight if possible.

4.2.4 Results of EOF Measurement Experiments

After amination, we need to find out the EOF magnitude in the NH_2-modified chips, but most importantly we need to verify that the direction of the electroosmotic flow is from the cathode to the anode. Here are the steps that proved that the flow is actually reversed as expected:

1- Fill the whole channel with the low concentration buffer.

2- Put the electrodes in

3- Wait till the flow stabilizes

4- Empty the anode and fill it up with the higher concentration buffer. This step needs to be done with delicacy to avoid the hydrodynamic influence.

5- Switch on the power supply and observe the current behavior.

If we get a stable signal, it means that there are no ions flowing from the anode to the cathode. The flow is therefore reversed. Then the electrodes are switched around. If the current is increasing, it indicates that the flow is going from the cathode towards the anode. The difference of voltage for this experiment was 475V. Using table 4.2, we conclude that the average electroosmotic mobility is $\boldsymbol{-1.271 \pm 0.12 cm^2/V.s}$ at a confidence level of 95%. The negative sign indicates that the mobility is reversed. . This value is very comparable to the one that has been listed before in the literature for aminated PMMA channels(Soper and McCarley, 2000).

Table4.2: EOF measurements of NH_2-PMMA

Iteration number	Observed $\Delta t(s)$	Calculated $\mu_e (cm^2/V.s)$
1	150	-1.26
2	152	-1.24
3	110	-1.72
4	123	-1.54
5	105	-1.8
6	225	-0.84
7	170	-1.11
8	122	-1.55
9	114	-1.67
10	150	-1.27
11	180	-1.05
12	181	-1.05
13	150	-1.26
14	174	-1.09
15	142	-1.34
16	182	-1.05
17	173	-1.10
18	152	-1.25
19	202	-0.94
20	148	-1.29

4.3. Process to Produce NH_2-Modified PC

As we achieved reversal of EOF for PMMA, the next step is to try the same surface modification principle on PC. This has not been done before using the amination method. We stated previously that this material is more suitable to the thermal cycling application of interest that the micro device would serve.

4.3.1 UV-Activation

Both the substrate bearing the micro-channel and the cover slips were exposed to UV-Light of a 254 nm light source for 30 min at 1 cm distance with a power density of 15 $mw.cm^{-2}$. The next step is to clean the micro device and the cover plate with distilled water, and dry them very well and very quickly afterwards before putting them in the oven.

4.3.2 Thermal Bonding

This step is exactly the same as described for PMMA, the only difference lies in the temperature for the bonding process. This temperature has been determined empirically to be around 148 degrees. We could not get good results using this temperature for 20 min so the temperature was raised up to 150 degrees and extended the exposure time in the oven to 30 min. We also ran the same checking tests as for PMMA after the micro-chips were out of the oven to see if they were ready to or not.

4.3.3 Amination

The solution that has been used for the amination of the PC was of 15 mM concentration. In 1 ml of phosphate buffer of pH=7, we added 45 μl of Ethylendiamine solution and 1mg of EDC. The final solution achieved was 15 mM.

We ran this solution into the UV-Activated channels using a syringe pump and let them stand for a couple of hours at least, preferable overnight if possible.

4.3.4 Results of the EOF Measurement

We ran the exact same test that we used previously for NH_2-PMMA and the flow was indeed from the cathode to anode. We used a voltage difference of 250V across a 3cm channel.

The table below shows the results for 20 EOF measurements.

Table4.3: EOF measurements of NH_2-PC

Iteration number	Observed $\Delta t(s)$	Calculated $\mu_e (cm^2/V.s)$
1	400	-0.9
2	450	-0.8
3	350	-1.02
4	127	-2.83
5	410	-0.87
6	341	-1.05
7	359	-1
8	411	-0.87
9	246	-1.46
10	402	-0.89
11	215	-1.67
12	196	-1.83

Table 4.3 continues in the next page

13	212	-1.69
14	242	-1.48
15	233	-1.54
16	174	-2.06
17	252	-1.42
18	310	-1.16
19	252	-1.42

We conclude that the average electroosmotic mobility is $-1.366 \pm 0.24 cm^2/V.s$ at a confidence level of 95%.

4.4. Pristine PC

After verifying the efficiency of the surface modification method on PC, we needed to have a reference value of mobility for the unmodified PC. The following process was used to produce pristine PC micro-channels and measured their mobility.

4.4.1 Thermal Bonding

This step is exactly the same as described for PMMA, the only difference lies in the temperature that was used for the thermal bonding. It has been determined empirically to be around 150 degrees. We also need to run the same checking tests as for PMMA after the micro-chips are out of the oven to see if they are ready to or not.

4.4.2 Results of the EOF Measurement

We used a voltage difference of 210V across a 3cm-long channel for the EOF measurement in the pristine PC channels. Table 4.4 below shows the results for 20 EOF measurements. Using table 4.4, we conclude that the average electroosmotic mobility is $3.934 \pm 0.8 cm^2/V.s$ at a confidence level of 95%.

Table4.4: EOF measurements of PC

Iteration number	Observed $\Delta t(s)$	Calculated $\mu_e (cm^2/V.s)$
1	117	3.648
2	276	1.539
3	80	5.358
4	122	3.515
5	158	2.717
6	150	2.85
7	120	3.572
8	197	2.185
9	144	2.964
10	128	3.344
11	78	5.491
12	45	9.519
13	119	3.519
14	189	2.28
15	96	4.465
16	121	3.534
17	134	3.192
18	78	5.491
19	90	4.75
20	90	4.75

Chapter 5.Conclusions and Recommendations

This work has been focused on theoretical analysis and numerical simulations of a modified micro-scale electrophoretron previously realized on the macro-scale and adapted here for cycling reactions applications. Experimental feasibility of the device has also been investigated by measuring the electroosmotic mobility properties of PMMA and PC and developing and testing a surface modification protocol necessary for the physical realization of the device.

The electrophoretron consists of a closed loop microchannel of arbitrary cross-section. If one part of the channel has an electroosmotic mobility of opposite sign than the remaining part, a continuous cyclic motion of the fluid in the closed loop channel can be sustained if a potential difference is applied on two electrodes strategically placed along the closed loop channel. Conservation of mass leads to formation of a pressure gradient and a related hydrodynamic flow. Our theoretical analysis shows how to minimize the hydrodynamic effects via a judicious choice of geometrical parameters as a function of the channel branch mobilities. We have identified a broad operating parameter feasibility window and, through numerical simulations, have shown that the device is feasible under realistic conditions including the effects of the presence of electrodes, bends, and practically achievable mobilities. The operating window is broad enough to accommodate manufacturing uncertainties in geometry and surface modification.

The benefits of this technology for application to the thermal cycling reactors are of importance. It eliminates long channel lengths, and consequently the associated pressure drop in a continuous flow device. Similarly it eliminates the associated high

voltage in electrokinetically driven microdevices. It minimizes thermal cycling and transition times and offers the flexibility of choosing the number of cycles desired without modifying the architecture of the device. It also relives from detection systems that are in use in traditional electrokinetically driven PCR reactors in order to track the species motion throughout different temperature zones.

The numerical simulations showed the proof of concept. The experimental proof of successful surface modifications of PC and PMMA demonstrated the feasibility of the process and the availability of potential materials that can be used for manufacturing the modified-electrophoretron.

Future study could focus on manufacturing such a device. It should address practical issues such as degasification of the chip due to electrolysis as well as the architecture and placement of the electrodes and of inlet and outlet ports.

References

1. Margolzata A Witek, Suying Wei, Bikas Vaydia, Andre A. Adams, Li Zhu, Wieslaw Stryjewski, Robin A. McCarley, Steven A.Soper, (2004), "Cell transport via electromigration in polymer-based microfluidic devices", submitted to Lab On A Chip.

2. Joong Gill Choi, Myieon Kim, Rajeev Dadoo, Richard N.Zare, (2001), "Electrophoretron: A New Method for Enhancing Resolution in Electrokinetic Separations, submitted to Journal of Chromatography A, 924, 53-58

3. Robin L.McCarley, Bikas Vaydia, Suying Wei, Alison F.Smith, Ami B.Patel, Juan Feng, Michael C.Murphy, Steven A.Soper, (2004), "Resist-Free Patterning of Surface Architectures in Polymer Based Micro-Analytical Devices", submitted to JACS communications

4. Hamed Shadpour, Harrisson Musyimi, Jifeng Chen, Steven A.Soper, (2006), "Physicochemical properties of various polymer substrates and their effects on microchip electrophoresis performance", submitted to Journal Of Chromatography A, 1111, 238-251

5. Jifeng Chen, Musundi Wabuyele, Hengwu Chen, Donald Patterson, Mateusz Hupert, Hamed Shadpour, Dimitris Nikitopoulos, Steven A. Soper, (2005), "Electrokinetically Synchronized Polymerase Chain Reaction Microchip Fabricated in Polycarbonate", submitted to Analytical Chemistry, 77, 658-666

6. Alyssa C.Henry, Tumari J.Tutt, Michelle Galloway, Yolanda Y.Davidson, C.Scott McWhorter, Steven A.Soper, Robin L.McCarley, (2000), Analytical Chemistry, 72, 5331-5337.

7. D.B. Holmes, J.R. Vermeulen, Velocity Profiles in Ducts with Rectangular Cross Sections. Chem. Eng. Sci.23, pp.717-722 (1968).

8. Jason L.Pittman, Charles S.Henry, S.Douglass Gilman, (2003), "Experimental Studies of Electroosmotic Flow Dynamics in Microfabricated Devices during Current Monitoring Experiments", Analytical Chemistry, 75, 361-370

9. M. Hashimoto, P. Chen, M.W. Mitchell, D.E. Nikitopoulos, S.A. Soper and M.C. Murphy. Rapid PCR in a Continuous Flow Device. *Lab on a Chip*, 2004, *4* , 638-645

Appendix A: EOF Measurements

EOF measurements for PC excel sheet

1	117	3.648
2	276	1.539
3	80	5.358
4	122	3.515
5	158	2.717
6	150	2.85
7	120	3.572
8	197	2.185
9	144	2.964
10	128	3.344
11	78	5.491
12	45	9.519
13	119	3.519
14	189	2.28
15	96	4.465
16	121	3.534
17	134	3.192
18	78	5.491
19	90	4.75
20	90	4.75
Dv=210V	Dv=210V	Dv=210V

3.9342
1.7234 43%
0.806 95%

EOF measurements for NH2-modified PC excel sheet

1	400	-0.9
2	450	-0.8
3	350	-1.02
4	127	-2.83
5	410	-0.87
6	341	-1.05
7	359	-1
8	411	-0.87
9	246	-1.46

10	402	-0.89
11	215	-1.67
12	196	-1.83
13	212	-1.69
14	242	-1.48
15	233	-1.54
16	174	-2.06
17	252	-1.42
18	310	-1.16
19	252	-1.42
DV=250	DV=250	DV=250

		-1.36632	
		0.513574	37.58821 %
	conf.		
	Interval	+/-	0.247544 95%

EOF measurements for PMMA excel sheet

1	102	2.18
2	116	1.9
3	108	2.04
4	104	2.12
5	200	1.05
6	263	0.81
7	112	1.97
8	75	2.96
9	367	0.58
10	126	1.75
11	101	2.18
12	109	2.02
13	101	2.18
14	136	1.62
15	141	1.56
16	75	2.92
17	72	3.07
18	70	3.15
19	84	2.62
20	125	1.76
DV=405	DV=405	DV=405

2.022

0.708138	35%
0.33	95%

EOF measurements for NH2-modified PMMA excel sheet

1	150	-1.26
2	152	-1.24
3	110	-1.72
4	123	-1.54
5	105	-1.8
6	225	-0.84
7	170	-1.11
8	122	-1.55
9	114	-1.67
10	150	-1.27
11	180	-1.05
12	181	-1.05
13	150	-1.26
14	174	-1.09
15	142	-1.34
16	182	-1.05
17	173	-1.1
18	152	-1.25
19	202	-0.94
20	148	-1.29
DV=475	DV=475	DV=475

-1.271	
0.264314	20.79%
0.12	95%

Appendix BMatlab Program for Concentration Average Vs. Time

```
%Tecplot 10 compatible code for estimating average concentration,given slice data
files
% clear all
% clc
% for f=1:6
% input=['nada',int2str(f),'.','txt'];  % inputting files at each time step
% fid=fopen(input,'r');
% %fid=fopen('data.txt');
% % fida=fopen('data_without_text.txt','w');% writing file without text
% % fidr=fopen('connectivity.txt','w');%putting the connectivity
% i=1;
% c=0;
% n=5;%19 is the number of variables at each node
% constant=0;
% tempsum=0;
% tempvar=0;
% ident=5;
% par=5; % first four lines are text and the fifth line contains data .hence value of
par=5;
% x_sum=0;
% y_sum=0;
% %writing the data without  text
% while (feof(fid)==0)
%   a=fgetl(fid);
%    wr(i)=cellstr(a);
%    text=str2num(char(wr(i)));
%    [pq rs]=size(text);
%    if(rs==0)
%       constant=constant+1;
%    end
%     i=i+1;
% c=c+1; %the final value of "c" gives the number of lines in the data file.
% end
%  num=constant/4;% estimating the no of slices  its divided by 4 since four lines of
text are there in tecplot 10
%
%
%
%
%  for ii=1:num
%
%  am=str2num(char(wr(par)));
%   [m n]=size(am);
%
```

```
%   while(n==5)
%      am=str2num(char(wr(par)));
%         [m n]=size(am);
%   par=par+1;
%   x_sum=x_sum+1;
% end
% nodes(ii)=x_sum-1;          %calculating the number of nodes for each slice
% x_sum=0;
% while(n==4&par<=c)
%     am=str2num(char(wr(par)));
%         [m n]=size(am);
%   par=par+1;
%   y_sum=y_sum+1;
% end
% elem(ii)=y_sum;            %  calculating the number of elements for each slice
% y_sum=0;
% if(n==0)
%     par=par+3;
% end
% end
% elem(num)=elem(num)+1;
%
%
% tot_sum=elem+nodes;
% elem_node_sum=0;
%
%
%
% %Actual program starts here
% for i_var=1:num
%
%   fida=fopen('data_without_text.txt','w');% writing file without text
%   fidr=fopen('connectivity.txt','w');%putting the connectivity
%            for j_var=ident:(nodes(i_var)+elem_node_sum+(4*i_var))
%
%               fprintf(fida,'%s  \n',char(wr(j_var)));           %writing data without
text
%
%             end
%
%             for k_var=j_var+1:(j_var+elem(i_var))     %writing connectivity list
%
%      fprintf(fidr,'%s  \n',char(wr(k_var)));
%
%   end
% elem_node_sum=elem_node_sum+tot_sum(i_var);
```

```
% ident=k_var+5;
%  fclose(fida);
%    fclose(fidr);
%
%      data=load('data_without_text.txt');%loading the slice FE data
%   b=load('connectivity.txt');%loading the connectivity list
% sum=0;
% init=0;
% [i j]=size(data);%i is the no of nodes in  the file
% [k L]=size(b);% no of elemets or the length of the connectivity list
% rows=i;
% co=data(:,j); %where j is the column number of species concentration at all the
nodes
% % xc=data(:,1); % This is the x cordinate location for nada's code to exclude the
nodes which are not required
% % ss=0;
% % for mm=1:k
% %
% %     for nn=1:1
% %
% %         if xc(bb(mm,nn),1)>0 % If the sign is ">"then left slice is calculated and
if "<" right slice is calculated
% %             ss=ss+1;
% %             cc=ss;
% %             b(cc,:)=bb(mm,:);
% %             ss=cc;
% %         end
% %     end
% % end
% % [k L]=size(b);
%
% for m=1:k%scanning through the connectivity list
%
%     for n=1:L
%         sum=sum+(1/4)*co(b(m,n),1);%calculating average concentration for an
element
%     end
%
%     d(m,1)=sum; %array for concentration after doing the average
%       sum=0;
%     for n=1:L%finding out the locations for each node in each row of connectivity
list
%         x(n,1)=data(b(m,n),1);
%         z(n,1)= data(b(m,n),3);
%     end
%  q=max(x);
```

```
%  r=min(x);
%  w=max(z);
%  g=min(z);
%
%
%     da(m,1)=(q-r)*(w-g);%calculating area of each element
%  end
%  p=(d.*da); %summing concentration over the cross section
%
%   sz=size(p);
%   tempsum=tempsum+1;
%  for s=1:sz
%    init=init+p(s,1);
% end
% a_slice=(max(data(:,1))-min(data(:,1)))*(max(data(:,3))-min(data(:,3)));
%calculating the area of the slice
% cavg(tempsum,1)=init/7500; %finding out the average concentration
% init=0; %initializing zero for next slice average
% y_p(tempsum,1)=data(1,2);
% plot(y_p(tempsum,1),cavg(tempsum,1))
% hold on
% for sigma=1:k
%     d(sigma,1)=0;          %initializing d and da to zero
% end
% for const=1:k
%     da(const,1)=0;
% end
%
% end
% mul(:,:,f)=cavg; % STORING ALL THE AVERAGED CONC'S IN EACH
COLOUMN FOR EACH TIME STEP ALONG THE LENGTH
%
% %   load handel
% %   sound(y,Fs)
% fclose(fid);
%  plot(y_p,cavg) %USE THIS FOR MISMATCH SIMULATIONS
% hold on
%
% end


% HERE THE MULTIDIMENSIONAL ARRAY "MUL" is converted to MATRIX
FORM TO BE
% % WRITTEN TO EXCEL SHEET
first_col=mul(:,:,1); % Taking the first coloumn or the avg conc values at first time
step to concatenate with the next timesteps
```

```
for kk=2:6
   concat_matrix=cat(2,first_col,mul(:,:,kk)); % succesive coloumns concatenated
and stored in a matrix
   first_col=concat_matrix;
end
excel_matrix=concat_matrix; % Storing in a matrix named EXCEL_MATRIX
xlswrite('C:\Documents and
Settings\Administrator\Desktop\15_33500_c_bis\AVG_CONC_33500_c.XLS',excel_
matrix) % Writing the Avg conc files at all time steps into the excel sheet in the
WORK DIRECTORY

load handel                % program ends and music is played with the help of this
command
  sound(y,Fs)
```

Vita

Nada was born on April 24th in Tangiers, Morocco. She Obtained Her “Baccalaureat Sciences-Maths” with honors in June 2000.

After two years of post-secondary program leading to the French competitive examinations to “Grandes Ecoles “she entered L’Ecole Nationale Superieure d’ Ingenieurs en Constructions Aeronautiques, an aerospace engineering school located in Toulouse, France.

She convinced her school to let her study abroad for her last year as an exchange student in order to get a Master of Science in Mechanical Engineering.

Nada enrolled a Master of Science Program in Mechanical Engineering in August 2004 at Louisiana State University in the Mechanical Engineering department with Dr. Dimitris E. Nikitopoulos as major professor. Her research was about designing an electrophoretron. She will be graduating in December 2006.